Orographic Influence on Basic Flow and Cyclone Circulation and Their Impacts on Track Deflection of an Idealized Tropical Cyclone

YUH-LANG LIN

Department of Physics, and Department of Energy and Environmental Systems, North Carolina A&T State University, Greensboro, North Carolina

SHU-HUA CHEN

Department of Land, Air, and Water Resources, University of California, Davis, Davis, California

LIPING LIU

Department of Mathematics, North Carolina A&T State University, Greensboro, North Carolina

ABSTRACT

A series of idealized numerical experiments and vorticity budget analyses is performed to examine several mechanisms proposed in previous studies to help understand the orographic influence on track deflection over a mesoscale mountain range. When an idealized tropical cyclone (TC) is embedded in a uniform, easterly flow and passes over a mountain with a moderate Froude number, it is deflected to the south upstream, moves over the mountain anticyclonically, and then resumes its westward movement. The vorticity budget analysis indicates that the TC movement can be predicted by the maximum vorticity tendency (VT). The orographic effects on the above TC track deflection are explained by the following: 1) Upstream of the mountain, the easterly basic flow is decelerated as a result of orographic blocking that causes the flow to become subgeostrophic, which advects the TC to the southwest, analogous to the advection of a point vortex embedded in a flow. The VT is primarily dominated by the horizontal vorticity advection. 2) The TC passes over the mountain anticyclonically, mainly steered by the orographically generated high pressure. This makes the TC move southwestward (northwestward) over the upslope (lee slope). The VT is mainly contributed by the horizontal vorticity advection with additional contributions from vorticity stretching and the residual term (which includes friction and subgrid turbulence mixing). 3) Over the lee slope and downstream of the mountain, the northwestward movement is enhanced by asymmetric diabatic heating, making the turning more abrupt. 4) Far downstream of the mountain, the VT is mainly contributed by the horizontal vorticity advection.

1. Introduction

When a tropical cyclone (TC) passes over a mesoscale mountain range, its track and structure and the associated precipitation are often influenced by the orography. Since the rainfall distribution and maximum rainfall location are dictated by the storm track, it is important to understand the mechanisms that control the track deflection. The orographic influence on track deflection has been observed and investigated for hurricanes passing over the south-central Appalachians (e.g., Harville 2009; Rostom and Lin 2015), the Cordillera Central of Hispaniola (Bender et al. 1987), and the Sierra Madre of Mexico (Zehnder 1993; Zehnder and Reeder 1997). Similar research has focused on typhoons passing over Taiwan's Central Mountain Range (CMR) and the Cordillera Central of northern Luzon in Philippines (e.g., Wang 1980; Brand and Blelloch 1974; Chang 1982; Bender et al. 1987; Yeh and Elsberry 1993a, b; Lin et al. 1999, 2005, hereafter L05; Wu 2001; Lin and Savage 2011; Tang and Chan 2014, 2015; Lin et al. 2006; Jian and Wu 2008; Huang et al. 2011; Hsu et al. 2013; Wang et al. 2013; Wu et al. 2015). However, some

Corresponding author address: Dr. Yuh-Lang Lin, EES, North Carolina A&T State University, 302H Gibbs Hall, 1601 E. Market St., Greensboro, NC 27411.
E-mail: ylin@ncat.edu

fundamental dynamics of the orographic effects on TC track deflection are still not well understood.

Based on observations and numerical simulations [e.g., see brief review in Lin (2007) and Wu et al. (2015)], when a typhoon passes over the CMR from the east, it may be deflected to the north or south upstream of the mountain. Based on previous studies, the following effects have been proposed to explain the upstream track deflection: 1) cyclonic circulation effect (e.g., Chang 1982; Bender et al. 1987), 2) advection by orographically blocked basic flow (e.g., Yeh and Elsberry 1993a,b; L05), 3) channeling effect (e.g., Lin et al. 1999; Jian and Wu 2008; Huang et al. 2011), 4) asymmetric latent heating effect (e.g., Chan et al. 2002; Hsu et al. 2013; Wang et al. 2013; Tang and Chan 2014, 2015), 5) northerly asymmetric flow steering effect (Wu et al. 2015), 6) effect of terrain-induced beta gyres (Tang and Chan 2014, 2015), and 7) effect of approach angle and landing location (Lin and Savage 2011; Tang and Chan 2015; Liu et al. 2016). Note that the above list is not necessarily exhaustive and may not account for other effects, such as vertical shear. In this study, we will focus on examining the abovementioned effects with the exception of approach angle and landing location as these have been investigated in a separate paper (Liu et al. 2016). The remaining effects will be briefly reviewed below.

The cyclonic circulation effect was proposed by Chang (1982) to explain the northward deflection of typhoons passing over Taiwan's CMR. When the idealized TC moves near the mountain range from the east, a stronger easterly flow is formed north of the mountain range by the TC's outer circulation and the westerly wind south of the storm center is turned into southerly. Thus, a cyclonic circulation forms around the mountain. As a result, the storm accelerates and deflects to the north, passes over the mountain cyclonically, and moves to the southwest of the mountain. Chang suggested that the cumulus heating in the vicinity of the mountain is responsible for generating and maintaining a cyclonic circulation around the topography, which then helps steer the low-level storm center to pass over the mountain cyclonically. Additionally, Chang performed a vorticity budget analysis for the low-level airflow prior to landfall and proposed that 1) cumulus heating generates convergence to maintain the vorticity of the TC and 2) the horizontal advection of positive vorticity in conjunction with the leeside vortex stretching results in the mean positive vorticity around the mountain. Based on numerical simulations of an idealized TC passing over the real topography of CMR, Bender et al. (1987) found the northward track deflection upstream of the mountain, confirming that found in Chang (1982). They suggested

that the terrain-induced steering flow modification is the main cause of the typhoon track deflection over the CMR. Furthermore, they found that track deflection is reduced when the basic-flow speed is increased.

Yeh and Elsberry (1993a,b), based on a combined observational and numerical approach, found that 1) stronger (weaker) typhoons tend to deflect to the north (south) upstream of the mountain range, 2) the deflection tends to be larger for weaker and slower-moving typhoons, and 3) the upstream deflection also depends on TC size. In other words, the upstream TC deflection is mainly controlled by orographic blocking. Zonal deceleration and southward track deflection of the TC are explained by an enhanced blocking and deflection of the environmental flow advecting the cyclone.

Based on idealized numerical simulations of a vortex embedded in a dry, easterly flow passing over a mesoscale mountain, L05 found three regimes of TC tracks: 1) weak orographic blocking, continuous track with northward upstream deflection; 2) moderate orographic blocking, discontinuous track with northward upstream deflection and a secondary vortex formed over the southwest lee slope; and 3) strong orographic blocking, discontinuous track. More importantly, L05 proposed that the strength of orographic blocking may be measured or quantified by the basic-flow and vortex Froude numbers, U/Nh and V_{max}/Nh, respectively, and other nondimensional control parameters (e.g., h/L_x and smaller R/L_y, U/fL_x, and V_{max}/fR). Here, U is the basic-flow speed, N is the Brunt–Väisälä frequency, V_{max} is the maximum tangential velocity of the vortex, h is the mountain height, R is the radius of V_{max}, f is the Coriolis parameter, and L_x and L_y are the horizontal scales of the mountain in x and y directions, respectively. Based on the estimates of nondimensional parameters from previous observational and numerical simulations of real cases and their own idealized numerical simulations (their Table 1), L05 found that the orientation of track deflections (north or south) is controlled by U/Nh, while the track discontinuity is controlled by $V_{max}/Nh < 1.5$. Rostom and Lin (2015) found that the track discontinuity for extratropical cyclones passing over the south-central Appalachians is controlled by $V_{max}/Nh < 1.5$ and $V_{max}/fR < 4.0$.

The southward deflection of a drifting vortex upstream of the mountain as simulated in the studies of Lin et al. may also be explained by the conservation of potential vorticity (PV) due to orographic blocking on a drifting vortex embedded in a dry, stably stratified fluid flow, as depicted in Fig. 1. The high pressure over the mountain is generated by the adiabatic cooling associated with the basic flow climbing over the mountain (e.g., see Smith 1979; Lin 2007). The southward deflection of the basic flow may also be explained by the
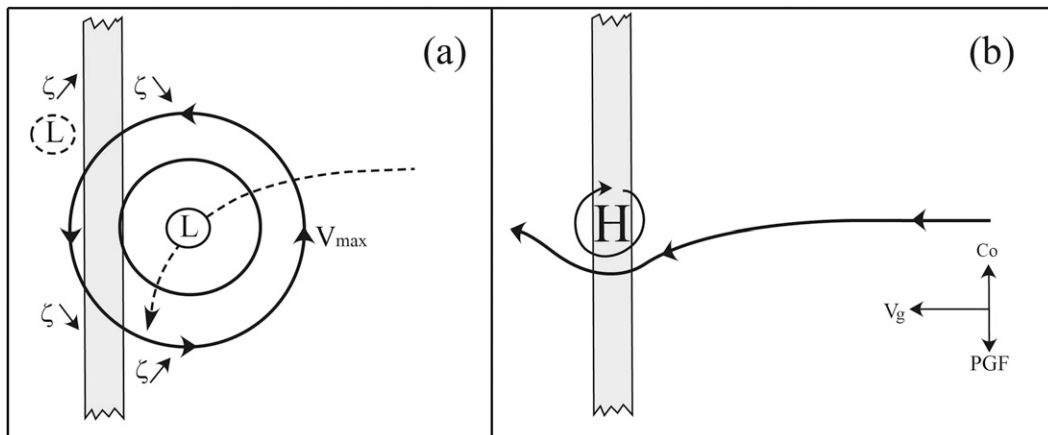
FIG. 1. A conceptual model for a TC vortex passing over a mesoscale mountain (V_g is geostrophic wind, Co is Coriolis force, and PGF is pressure gradient force). The southward (northward) deflection upstream (downstream) of the mountain is explained by the conservation of PV for (a) a dry vortex and (b) stably stratified fluid flow passes over a mountain range. [Adapted from Lin (2007).]

imbalance of geostrophic wind as the westward wind speed is reduced (i.e., subgeostrophic) by the orographic blocking mechanically, similar to that simulated by Chen and Lin (2005). A TC embedded in a moist airflow behaves significantly differently from a vortex drifting in a dry airflow and requires further investigation. In addition, PV associated with a TC and its true environment is not conserved because of latent heat release by cumulus convection and friction in the planetary boundary layer (PBL). In this study, Lin et al. (1999) and L05 are extended to include diabatic heating and the PBL to help understand their effects on TC track deflection when the storm passes over a mesoscale mountain.

The southward track deflection upstream of the mountain was explained by the advection of the orographically induced northerly jet between the mountain and TC vortex (Lin et al. 1999). This channeling effect has also been applied to explain the sudden southward deflection of Supertyphoon Haitang (2005) (Jian and Wu 2008) and Typhoon Krosa (2007) (Huang et al. 2011). Based on idealized numerical simulations, Wu et al. (2015) proposed that, unlike the channeling effect, the southward TC deflection upstream of the mountain is mainly caused by the northerly asymmetric flow in the midtroposphere. Wu et al. (2015) attributed the formation of the midtropospheric northerly asymmetric flow to the enhanced flow west of the storm center. While the asymmetric flow steering effect might provide an explanation of their numerical results, it remains unclear as to the source of this deep-layer asymmetry associated with the TC vortex when it approaches the mountain.

In addition to the above effects on track deflection, it has been found that when latent heating becomes asymmetric, the storm motion may be affected through PV generation and subsequent advection (e.g., Chan 1984; Fiorino and Elsberry 1989; Elsberry 1995; Wu and Wang 2001b; Chan et al. 2002). This type of asymmetric diabatic heating has been used to explain 1) the slow-down of Typhoon Morakot's (2009) motion after its postlandfall period in Taiwan (Wang et al. 2012); 2) the westward speedup of a slow-moving northern TC and a significant fraction of the slow-moving TCs affected by the convection phase locked to the topography upon their departure, such that their moving speeds were further reduced after they moved across the CMR; and 3) the faster and northwestward-moving TC after Typhoon Fanapi (2010) passing over the CMR owing to the existence of rainbands to the east and south (Wang et al. 2013).

The numerical model and experimental design will be introduced in section 2. The orographic impacts on track deflection for a uniform, easterly flow with an embedded TC passing over a mesoscale mountain range (case CNTL) will be investigated in section 3. A vorticity budget analysis is then performed in section 4 to help understand the mechanisms responsible for a TC's upstream deflection, which include cyclonic circulation, mean flow advection, northerly asymmetric flow steering, asymmetric latent heating, and vertical shear effects. In section 5, the upstream orographic influence on the basic flow and TC movement and its relation to the channeling effect will be investigated by analyzing the results of a moist (CNTL) flow with no TC (NOTC) and performing a dry flow with an embedded TC vortex

TABLE 1. Summary of numerical experiments.

Case	U (m s^{-1})	V_{max} (m s^{-1})	h_o (km)	Remarks[b]
CNTL	−5	21/55[a]	1	A vortex embedded in a uniform easterly flow over a mountain on an f plane
NOHT	−5	21/11	1	As in case CNTL, but for all heat fluxes deactivated (i.e., a dry case)
NOTC	−5	0	1	As in case CNTL, but for no TC
M500	−5	21/55	0.5	As in case CNTL, but for $h_o = 500$ m
NOMT	−5	21/55	0	As in case CNTL, but for no mountain
NOBL	−5	0	1	As in case CNTL, but for no PBL

[a] (Initial vortex V_{max})/(spun-up TC V_{max}).

[b] All cases have mountain geometry specified by Eq. (1) with $a = 100$ km (east–west length $= L_x = {\sim}4a$), $b = 800$ km (north–south length $= L_y = {\sim}b + 4a$), $f = 5.0 \times 10^{-5}$ s^{-1} (at 20°N), and $\beta = 0$ m^{-1} s^{-1}. Parameterization for microphysics is Purdue–Lin, for cumulus is Kain–Fritsch, for PBL is YSU, for surface layer is Monin–Obukhov, for land surface processes is unified Noah, and for long- and shortwave radiation is deactivated. Finally, $\Delta t = 45$ s; $\Delta x = \Delta y = 15$ km; horizontal domain size $= (6480, 6480$ km$)$; and total time $= 12$ days.

(NOHT) over a mountain. The concluding remarks can be found in section 6.

2. The numerical model and experimental design

The model used for this study is the Advanced Research version of the Weather Research and Forecasting (WRF) Model (ARW), version 3.4.1 (Skamarock et al. 2008). ARW is a fully compressible, three-dimensional, nonhydrostatic model using terrain-following vertical coordinates. The governing equations of ARW are written in flux form with conserved mass and dry entropy. In this study, the Runge–Kutta third-order scheme is used to integrate in time while the fifth- and third-order advection schemes are used to integrate horizontally and vertically in space, respectively. For numerical simulations, we utilize a single domain with a horizontal resolution of 15 km. The grid points are 433×433 in the x–y directions. In the vertical, there are

41 grid levels, which are stretched from the surface to the model top (${\sim}20$ km) with finer resolutions in the boundary layer. An open boundary condition is applied to the east and west lateral boundaries while a periodic boundary condition is applied to the north and south boundaries, following a point-downscaling approach proposed in Nolan (2011) that eliminates the geostrophic balance portion of the forces in the initial fields. A 4-km sponge layer is added to the top of the physical domain to damp the upward-propagating waves and those reflected from the model top. In all of our simulations, we have paid close attention to the flow fields near the lateral boundaries and found no obvious reflections of waves or disturbances. All simulations use only one domain. ARW integrates for 12 days with a time step Δt of 45 s.

An elongated, north–south-oriented, bell-shaped mountain range is placed in the domain. The mountain geometry is defined as the following:
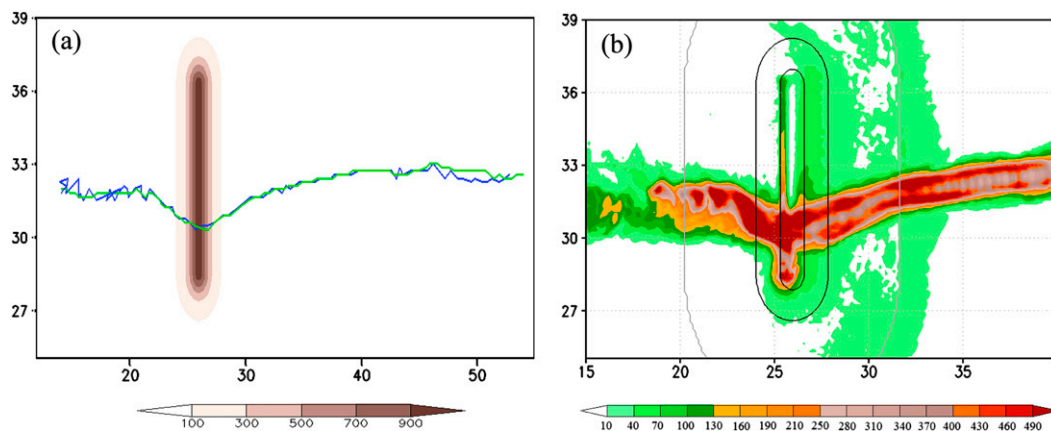

FIG. 2. For case CNTL, (a) tracks of P_{min} (green) and 850-hPa max VT (blue) of the bogus TC and (b) the accumulated rainfall (color shaded) in a zoomed-in domain. The mountain height is shaded in (a) and contoured in (b) [5 (gray), 100 (black), and 600 m (black)]. The abscissa and ordinate are labeled in 100 km from the southwest corner of the actual model domain. The center of the mountain is located at $(x_0, y_0) = (2595, 3240$ km$)$ or grid point (173, 216). The x and y domain size is 6495 km.
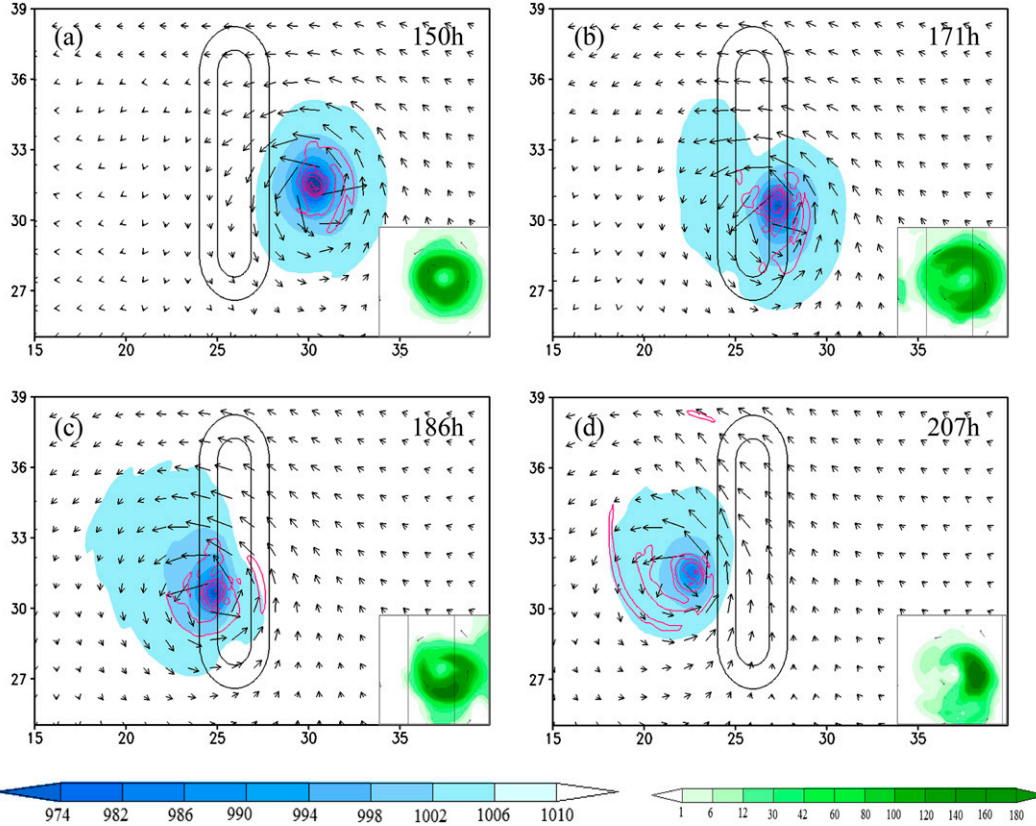
FIG. 3. For case CNTL, MSLP (shading), 850-hPa (σ surface) relative vorticity (contours in magenta), and vector wind fields at (a) 150, (b) 171, (c) 186, and (d) 207 h. The relative vorticity contours are 0.0001, 0.0005, 0.001, 0.002, and 0.003 s^{-1}. Insets are the 3-h accumulated rainfall (shaded in green). The mountain height contours are 100 and 600 m. The scale of the insets is enlarged to make the rainfall pattern more visible.

$$h(x, y) = \frac{h_0'}{[1 + (x - x_0)^2/a^2]^{3/2}} - h' \quad \text{for} \quad |y - y_0| \leq b/2,$$

$$(1a)$$

$$= \frac{h_0'}{[1 + (x - x_0)^2/a^2 + (y - y_1)^2/a^2]^{3/2}} - h' \quad \text{for}$$

$$y - y_0 < -b/2, \quad \text{and}$$

$$(1b)$$

$$= \frac{h_0'}{[1 + (x - x_0)^2/a^2 + (y - y_2)^2/a^2]^{3/2}} - h' \quad \text{for}$$

$$y - y_0 > b/2,$$

$$(1c)$$

Where $y_1 = y_0 - b/2$, $y_2 = y_0 + b/2$, $h_0' = h_0 + h'$, $h' = h_0/(5^{3/2} - 1)$, and h_0 is the height of the mountain range, $a = 100$ km, $b = 800$ km, and location $(x_0, y_0) = (2595, 3240$ km$)$ or grid point (173, 216) is the center of

the mountain. In this study, the mountain widths are $L_x = 4a$ and $L_y = b + 4a$ for all cases.

In the control experiment (i.e., CNTL), the initial and environmental conditions use a point-downscaling approach created by an offline code (Nolan 2011; Nolan et al. 2013) and are interpolated into ARW [Eq. (1)]. In the offline code, a bogus vortex with the maximum tangential wind (i.e., V_{max}) of 21 m s^{-1} and the radius of the maximum wind R of 100 km, which is in gradient wind balance, is initially inserted at $x = 5400$ km into an easterly flow of $U = -5$ m s^{-1} over a 1-km-high mountain. The vertical structure of the initial vortex is identical to that used in radiative–convective equilibrium studies. All simulations with a bogus vortex use a modified Rankine vortex with decay parameter 0.4 (Mallen et al. 2005) and a fixed sea surface temperature (SST) of 28°C. The land surface temperature is also fixed at 28°C. The domain is initialized with the "moist tropical" sounding used in Dunion (2011) and the horizontal temperature and moisture fields are homogeneous, except over the storm area. The domainwide wind profile
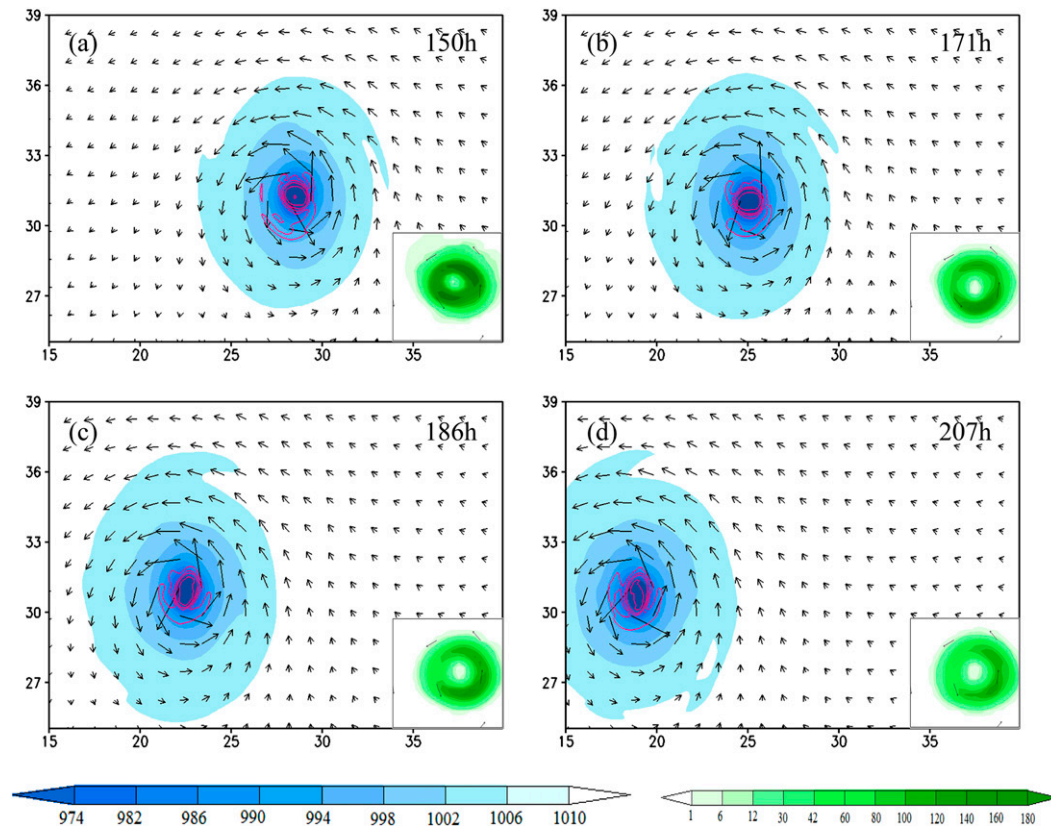
FIG. 4. As in Fig. 3, but for case NOMT. Insets are the rainfall distribution in the vicinity of the eyewall.

is purely zonal and uniform with $U = -5\,\mathrm{m\,s}^{-1}$. All simulations are on the f plane at 20°N with $f = 5.0 \times 10^{-5}\,\mathrm{s}^{-1}$ across the domain. In addition to the CNTL experiment, five other sensitivity experiments are performed, which are characterized by 1) NOHT [as in case CNTL except with all heat fluxes deactivated (i.e., a dry case)], 2) NOTC (as in case CNTL except no TC), 3) M500 (as in case CNTL except with the mountain height reduced to 500 m), 4) NOMT (as in case CNTL except with a flat terrain), and 5) NOBL (as in case CNTL except with no PBL). These numerical experiments are also summarized in Table 1. Since, as expected, case NOBL produces nearly no convection and rainfall the results are not shown. It is well known that the presence of the PBL is essential in producing the moisture convergence, providing surface fluxes of moisture and heat from the ocean, and playing important dynamical role in TC intensification (e.g., Smith and Thomsen 2010).

The physics parameterization schemes used for all experiments are Kain–Fritsch cumulus parameterization scheme (Kain and Fritsch 1993; Kain 2004), Purdue–Lin microphysics parameterization scheme [Chen and Sun (2002); based on Lin et al. (1983, hereafter LFO) and Rutledge and Hobbs (1984)], Yonsei

University (YSU) PBL parameterization scheme (Hong and Pan 1996), Monin–Obukhov surface layer scheme (Monin and Obukhov 1954), unified Noah land surface processes scheme (Tewari et al. 2004), and the second-order diffusion on coordinate surfaces. The long- and shortwave radiation parameterization schemes are deactivated. Details of the above schemes and their relevant references can be found in Skamarock et al. (2008).

3. Orographic effects on TC track and structure

In this section, several effects proposed in previous studies are examined, including the mean flow advection, cyclonic circulation, asymmetric diabatic heating, northerly asymmetric flow steering, and vertical shear effects. For case CNTL, the bogus vortex with $V_{max} = 21\,\mathrm{m\,s}^{-1}$ in the gradient wind balance is initially inserted into an easterly flow of $U = -5\,\mathrm{m\,s}^{-1}$ over a 1-km-high mountain [Eq. (1)]. The bogus vortex then gradually develops into a mature TC with $V_{max} = 55\,\mathrm{m\,s}^{-1}$ in about 100 h (also see Fig. 4, described in greater detail below). The basic-flow moist Froude number ($\sim$0.49) is defined as $U/N_w h$, where N_w is the unsaturated Brunt–Väisälä
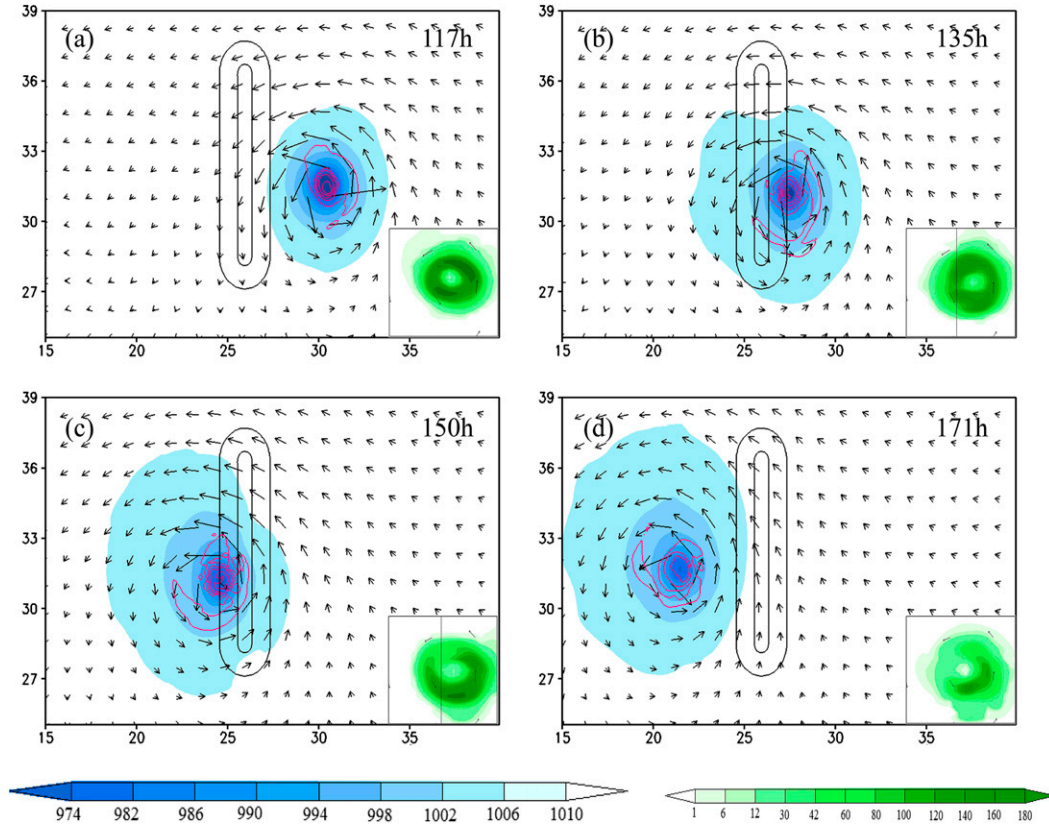
FIG. 5. As in Fig. 3, but for case M500 ($h = 500$ m) at (a) 117, (b) 135, (c) 150, and (d) 171 h. The mountain height contours in are 100 and 400 m.

frequency and h is the height of the mountain peak. The N_w is defined (Emanuel 1994; Chen and Lin 2005) as

$$N_w^2 = \frac{g}{\overline{\theta}_v} \frac{\partial \theta_v}{\partial z}, \qquad (2)$$

where g is the gravitational acceleration, θ_v is the virtual potential temperature, and z is the vertical coordinate. The tropical sounding (Dunion 2011) used in this study gives $N_w = \sim 0.0102 \, \text{s}^{-1}$, leading to the basic-flow and vortex Froude numbers $U/N_w h = \sim 0.5$ and $V_{\max}/N_w h = \sim 5.4$,
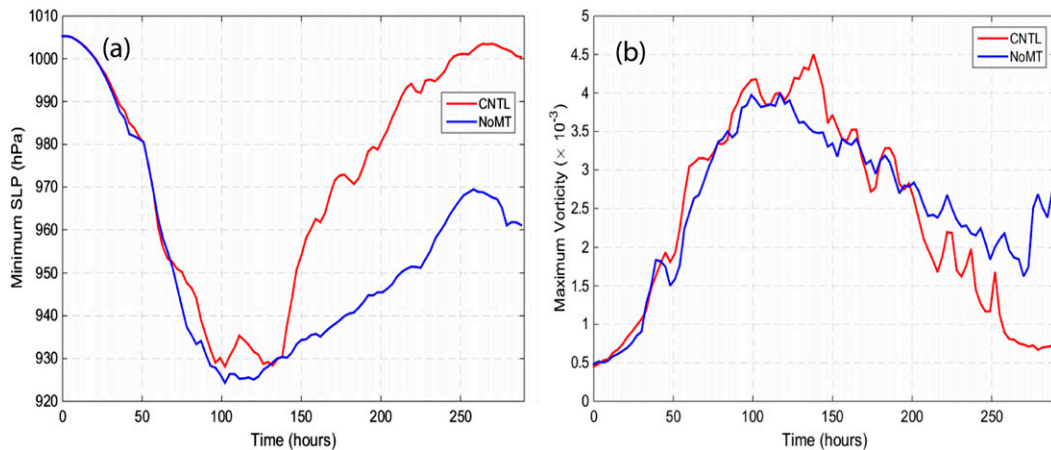
FIG. 6. Evolutions of time for (a) $P_{\min}$ and (b) 850-hPa max relative vorticity for cases CNTL (red) and NOMT (blue).
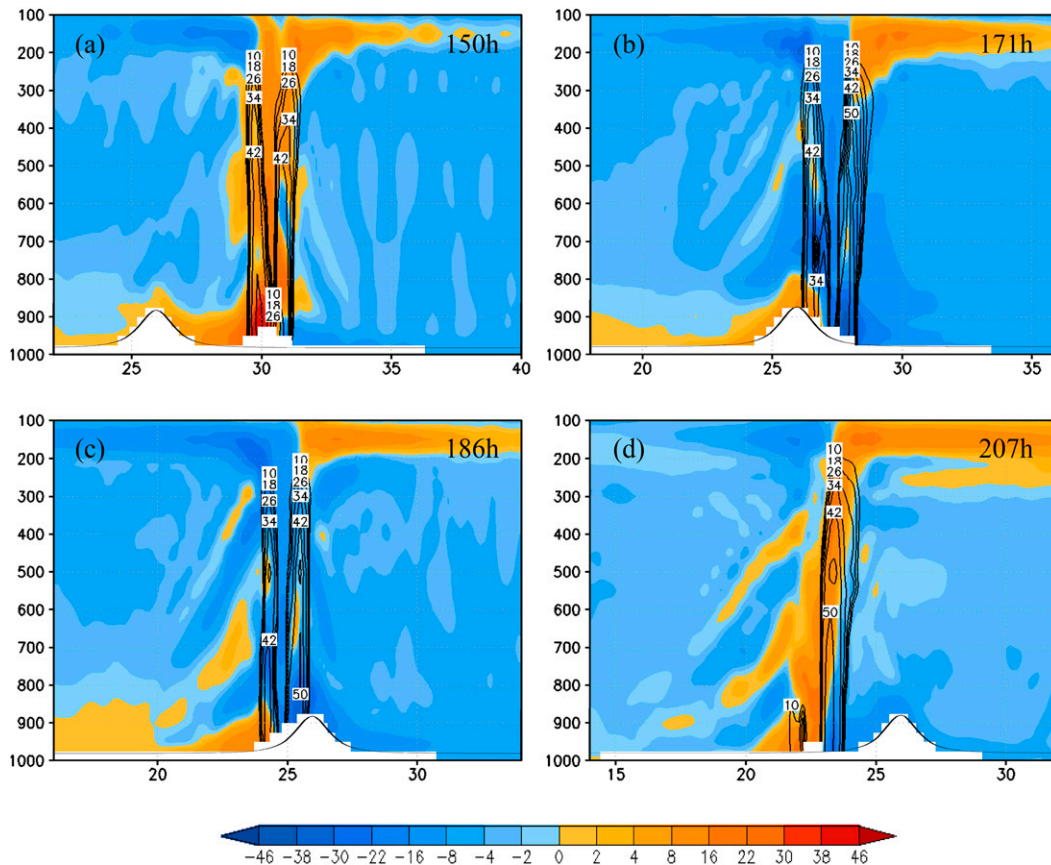
FIG. 7. For case CNTL, vertical sections of the U (east–west) wind component (m s^{-1}; shaded) and radar echoes (dBZ; contours) across the TC center at (a) 150, (b) 171, (c) 186, and (d) 207 h. The horizontal and vertical axes are in 100 km and hPa, respectively. The mountain range is centered at $x = 2595$ km.

respectively. Note that this sounding represents a typical tropical atmosphere that is almost moist neutral from 700 to 330 hPa. The sounding is conditionally unstable below 700 hPa and is quite moist near the surface. Since the convective available potential energy (CAPE) is relatively higher ($\sim$1765 J kg^{-1}) and the level of free convection (LFC) is relatively lower ($\sim$874 hPa), strong and deep convections can be initiated.

a. Orographic influence on TC track, intensity, and structure

The TC track following the minimum sea level pressure P_{min} is shown in Fig. 2a. The zigzag pattern of the track east of $x = 4500$ km is due to the spinup process from a bogus vortex to a mature TC. When the TC approaches the mountain from east, it is deflected to the south, passes over the mountain anticyclonically, and then resumes its westward movement downstream of the mountain. The track continuity is consistent with the moderate blocking regime as proposed in L05, because the basic-flow Froude number (i.e., U/Nh) and the

vortex Froude number (i.e., V_{max}/Nh) are 0.5 and 5.4, respectively. The mechanism for the track deflection will be explained later in this section and in sections 4 and 5. Note that the northward track deflection for the moderate blocking regime as proposed in L05 is, in their case, mainly due to the shorter north–south scale of the mountain and lack of latent heating and PBL effects. Figure 2a shows the track following the 850-hPa maximum vorticity tendency (VT; defined as $\partial \zeta / \partial t$, where ζ is the relative vorticity), which is almost identical to that tracked by P_{min} (Fig. 2a), the traditional variable used for TC tracing. Therefore, the TC path may also be tracked by VT.

The accumulated rainfall accompanying the TC (Fig. 2b) shows a path almost identical to the track represented by both the P_{min} and VT (Fig. 2a). Before reaching the upslope of the mountain at 150 h, the TC is able to keep its symmetry, as evidenced by the mean sea level pressure (MSLP), rainfall, and total wind patterns (Figs. 3a and 7a; Fig. 7a is described in greater detail below). Note that the southward deflection has started
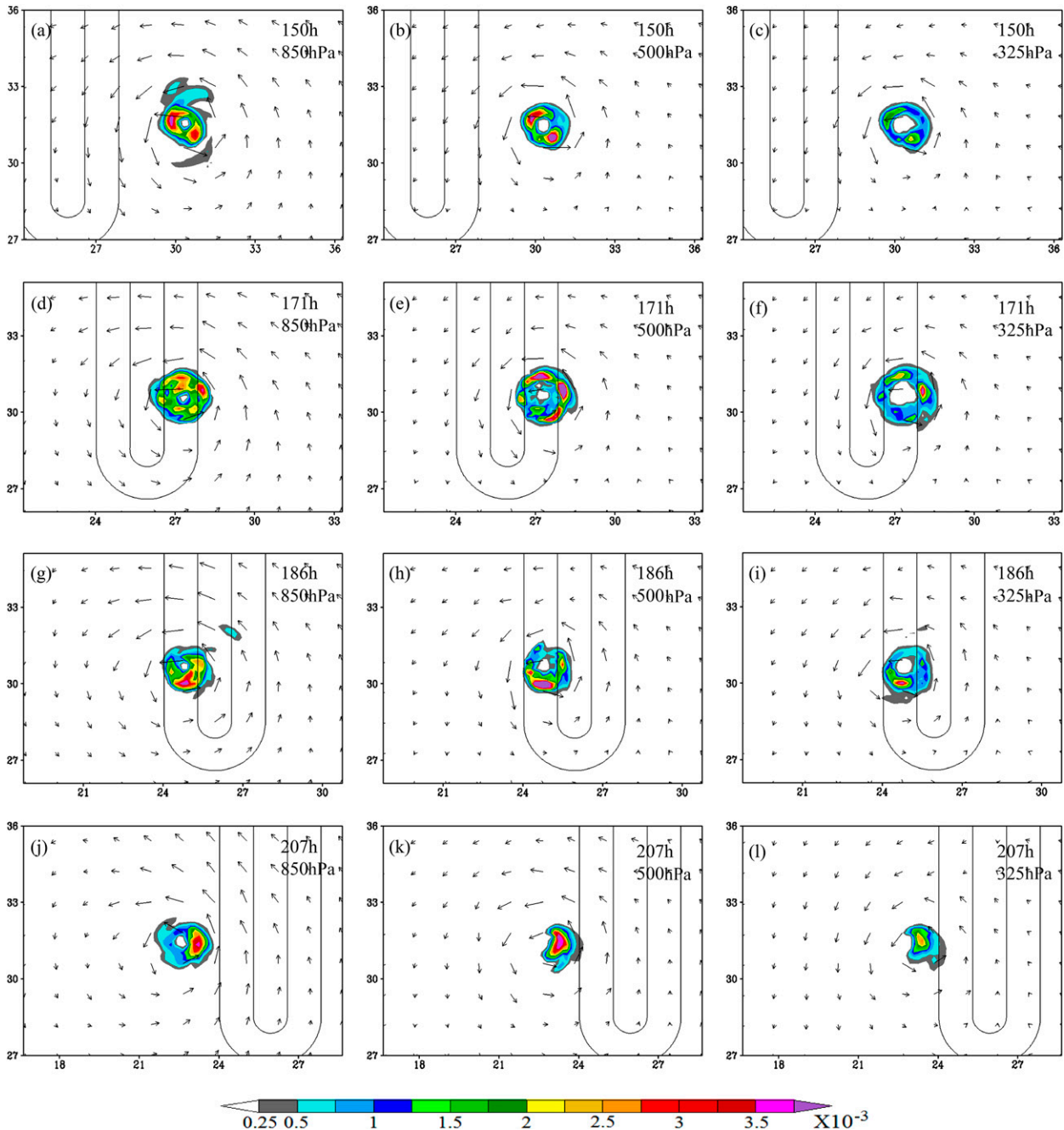
FIG. 8. For case CNTL, distributions of total water content at (left) 850, (center) 500, and (right) 325 hPa for the total water content (cloud) when the TC moves to (a)–(c) upstream of the mountain at 150 h, (d)–(f) over the upslope at 171 h, (g)–(i) over the downslope at 186 h, and (j)–(l) downstream of the mountain at 207 h.

much earlier than this time, implying that the northerly asymmetric flow steering effect proposed by Wu et al. (2015) does not seem to play a major role upstream of the mountain. However, this does not rule out its potential significance under different flow, mountain, and/or TC settings. The southward deflection of the TC starts near $x = 3300$ km, which is

about 700 km upstream of the mountain peak (Fig. 2b). The upstream influence of a mesoscale mountain can be estimated by the Rossby radius of deformation (Nh/f), which gives a distance of about 204 km (about $x = 3300$ km in the present case) with $N = N_w = 0.0102\,\mathrm{s}^{-1}$, $h = 1$ km, and $f = 5 \times 10^{-5}\,\mathrm{s}^{-1}$, based on Pierrehumbert and Wyman (1985). The difference may be due to the
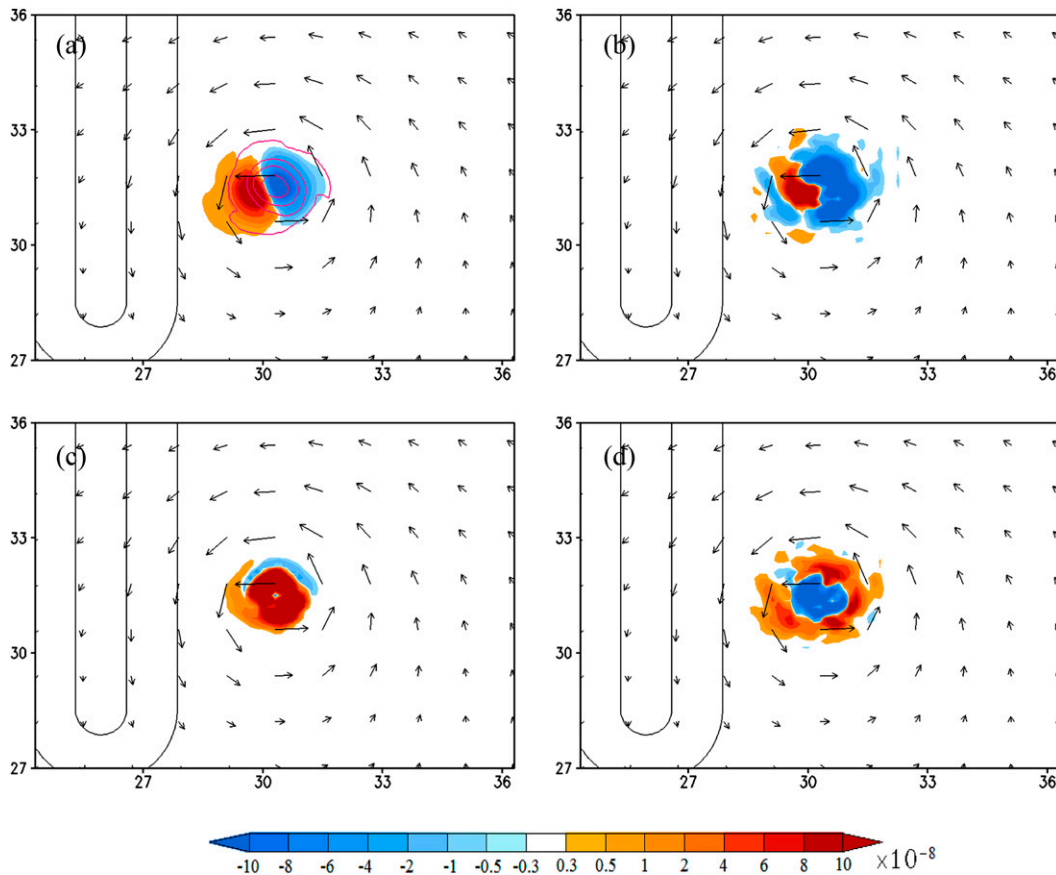
FIG. 9. For case CNTL, the surface–500-hPa-layer-averaged vector wind field and (a) VT and relative vorticity (contours in magenta), (b) horizontal vorticity advection, (c) vorticity stretching, and (d) residual term at 150 h. These terms are averaged over 147, 150, and 153 h.

dry and stable flow assumed in Pierrehumbert and Wyman's study. However, the orographically influenced rainfall, which reaches $x = 3400$ km (Fig. 2b), is about 800 km upstream of the mountain peak. This is more consistent with the upstream influence on track deflection and may be associated with the density current, which is able to push the orographic rainfall area farther upstream of $x = 3300$ km. Moreover, this agrees with earlier studies for typhoons passing over Taiwan's CMR where the effect of the mountain on typhoon tracks is as far as 800 km upstream [e.g., Fig. 11 of Yeh and Elsberry (1993a,b)].

The storm symmetry is disrupted by orographic blocking when the TC moves over the mountain. This is observed particularly along the upslope (Fig. 3b), lee (western) slope (Fig. 3c), and downstream of the mountain (Fig. 3d), as revealed in the MSLP and rainfall patterns (cf. to those upstream of the mountain in Fig. 3a). The MSLP and rainfall patterns from cases no mountain (i.e., NOMT) (Fig. 4) and 500-m-high mountain (i.e., M500) (Fig. 5) show a similar effect on symmetry. When

the TC moves over the upslope, the western flank of the eyewall convection is severely weakened by orographic forcing, as shown in the accompanied rainfall pattern (Fig. 3b). As revealed by the $P_{\min}$ (Fig. 6a) and the 850-hPa maximum relative vorticity $\zeta_{\max}$ (Fig. 6b) of case NOMT, the storm asymmetry is also partially due to the natural evolution of the TC intensity. Note that in case NOMT, it takes about 100 h for the initial bogus vortex with $P_{\min} = 1005$ hPa and $\zeta_{\max} = 5 \times 10^{-4}\,\text{s}^{-1}$ to spin up to its mature stage with $P_{\min} = 930$ hPa and $\zeta_{\max} = 3.8 \times 10^{-3}\,\text{s}^{-1}$ (Fig. 6). The TC sustains its intensity from 100 to about 120 h, and then starts to weaken gradually to about 968 hPa and $2.0 \times 10^{-3}\,\text{s}^{-1}$ at 250 h. Since no mountain is present in this case, the behavior of the $P_{\min}$ and $\zeta_{\max}$ is due to the TC's natural evolution of structure and intensity. These last characteristics are mainly controlled by the storm's internal dynamics, such as PBL and convective cloud processes. In case CNTL, it is difficult to differentiate the contributions from orographic blocking and natural evolution since these processes are highly nonlinear. Therefore, one
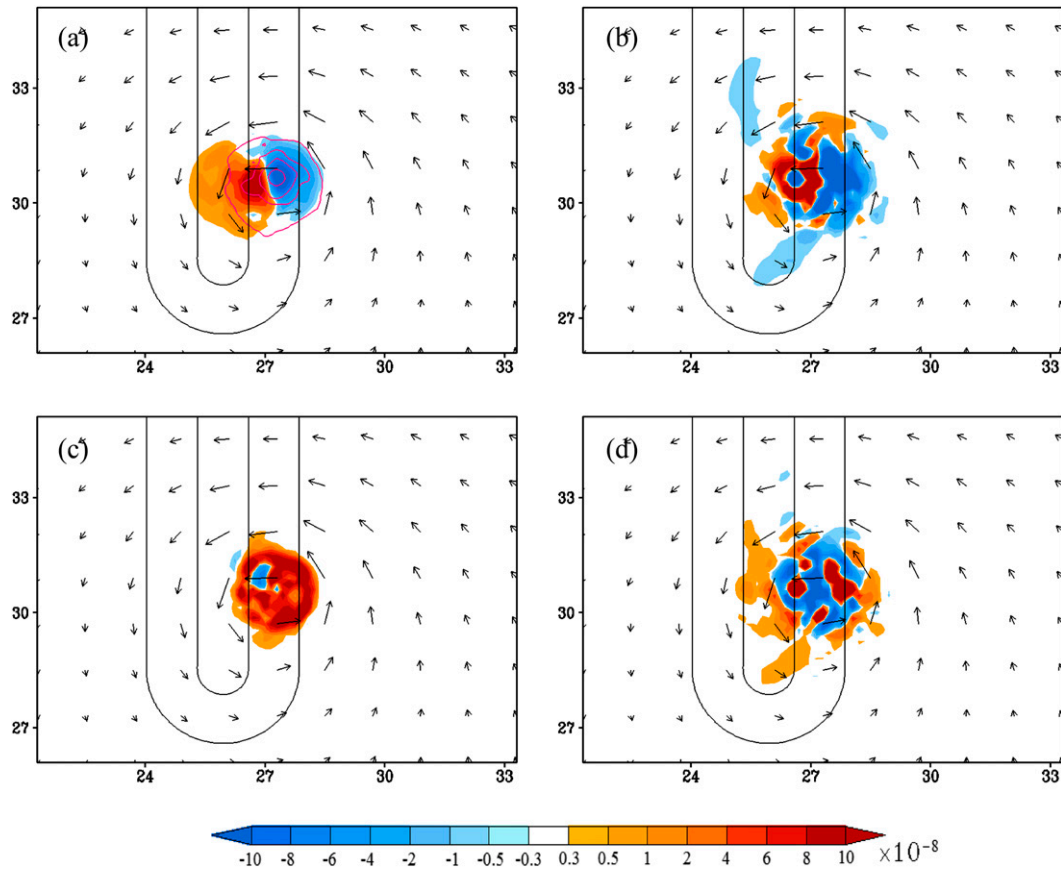
FIG. 10. As in Fig. 9, but for 171 h.

cannot simply take the differences between the blue and red curves in Fig. 6 as being indicative of a single contributor.

The P_{min} in case CNTL starts to increase rapidly after about 140 h and is much higher than that in case NOMT (Fig. 6), indicating the effect of orographic blocking on TC intensity. From 140 to 200 h when the TC is moving over the mountain, unlike the P_{min}, the ζ_{max} keeps oscillating at a period of about 10 h before it decreases dramatically after about 200 h. This relatively rapid oscillation appears to be more related to mechanical forcing since it does not occur with P_{min}.

Another significant orographic influence on the TC is the reduction of the zonal moving speed due to orographic blocking, which is $\sim$3.66 m s^{-1} as estimated from 150 to 207 h for case CNTL (Fig. 3) versus $\sim$4.85 m s^{-1} for case NOMT (Fig. 4). A close inspection of Fig. 4 reveals that the TC is moving slightly southward, which can be explained by the blocking effect of the TC on the easterly basic flow ($-$5 m s^{-1}). Note that the TC is moving at about 4.85 m s^{-1} westward, based on an estimate from Figs. 4a–d, which is slower than the basic flow. Thus, there exists an easterly basic flow of 0.15 m s^{-1} in

the reference frame moving with the TC. This will decelerate the basic flow to the east of the TC, analogous to the conceptual model of Fig. 1b, and make the basic easterly flow relative to the TC (i.e., $U = -0.15$ m s^{-1}) subgeostrophic. This subgeostrophic flow will produce a smaller Coriolis force and an imbalance between the Coriolis force and pressure gradient force to steer the TC to the south. For case M500 ($h = 500$ m), the orographic influence on track deflection, rainfall distribution, and wind field (Fig. 5) is similar to case CNTL except it is weaker and the storm is able to maintain its symmetry over the upslope.

The evolution of TC intensity and U (east–west) wind component in case CNTL can be seen from the model-simulated radar reflectivity on the east–west vertical cross section through the TC center (Fig. 7). At 150 h, when the TC is upstream of the mountain before landfall, the eyewall convection is approximately symmetric (Figs. 7a and 3a). At 171 h, when the TC moves to upslope, it becomes asymmetric when the western flank of the eyewall broadens and splits into two weaker convective cells (Fig. 7b). Meanwhile, the eastern flank of the eyewall deepens and intensifies (Fig. 7b), resulting in
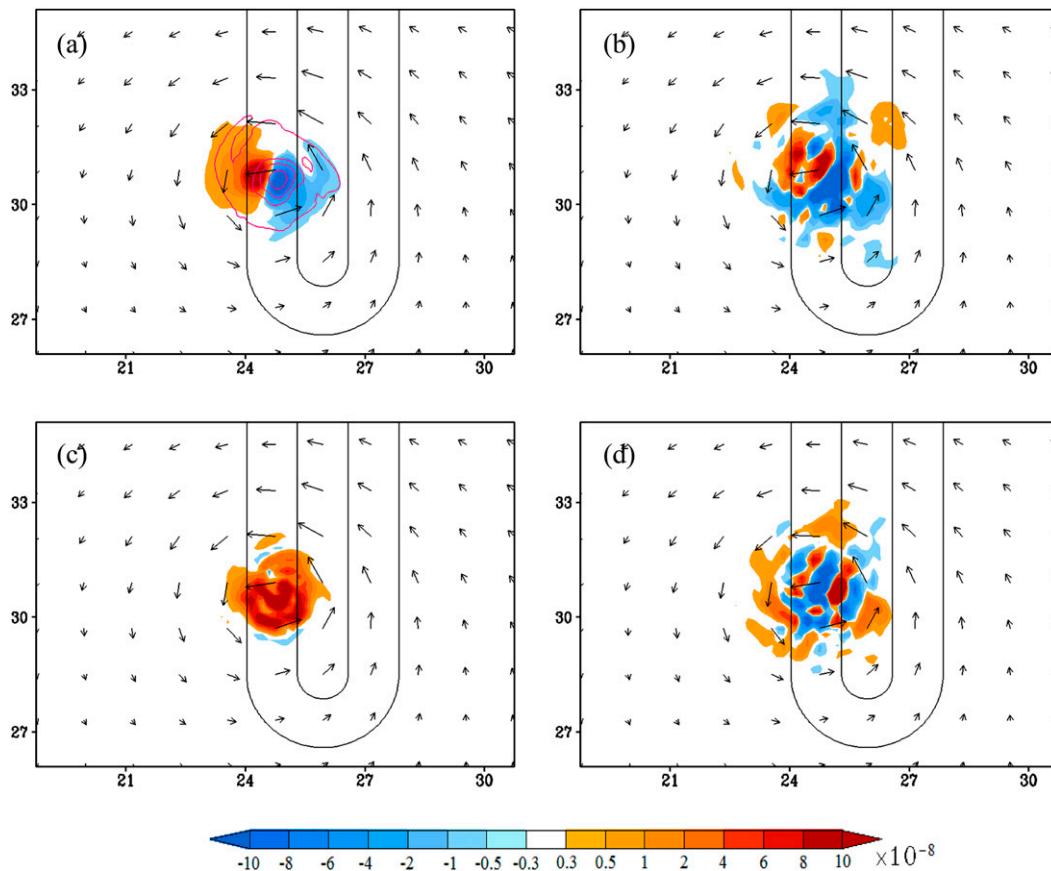
FIG. 11. As in Fig. 9, but for 186 h.

the maximum rainfall over the eastern flank of the storm (Fig. 3b). The western flank of the eyewall is significantly weakened by the mountain after the TC passes over the peak at 186 h (Fig. 7c). At 207 h, the western flank of the eyewall becomes very weak and shallow (Fig. 7d). Overall, as revealed in Figs. 3–5 and 7, the TC is able to keep its symmetrical structure upstream of the mountain (e.g., 150 h; Fig. 7a), but becomes slightly asymmetric over the upslope (e.g., 171 h; Fig. 7b). The storm becomes significantly asymmetric and weakened after passing over the mountain peak to the downslope (e.g., 186 h; Fig. 7c) and downstream of the mountain (e.g., 207 h; Fig. 7d).

b. Effects of asymmetric diabatic heating and asymmetric flow steering, and vertical shear on TC track

When a TC moves over a mountain, the asymmetric diabatic heating discussed above may occur at different levels, as revealed in the asymmetric distributions of the total water content, which represent cloud or approximately PV areas (Fig. 8). Upstream of the mountain and over the upslope, the cloud areas of the TC at 850

(Figs. 8a,d) and 500 hPa (Figs. 8b,e) are less symmetric compared to that for 325 hPa (Figs. 8c,f), owing to stronger orographic blocking in the lower layer. Overall, the cloud areas are less symmetric compared to the 3-h accumulated rainfall (Fig. 3a) owing to rapid temporal evolution of complicated cloud processes. The cloud asymmetry becomes more pronounced with more total water content to the east and south of the vortex center after the TC passes over the mountain peak. This is seen over the lee slope (Figs. 8g–i) and downstream of the mountain (Figs. 8j–l and 7d). The slightly more abrupt northwestward movement downstream of the mountain (Fig. 2a), compared to the southwestward movement upstream of the mountain, can be explained by the asymmetrical diabatic heating as represented in the asymmetric total water content (cloud). This is similar to that found in simulations of Typhoon Fanapi (2010) by Wang et al. (2013). As briefly reviewed in the introduction, the asymmetric diabatic heating effect on the storm motion is through the generation of PV and its subsequent advection (e.g., Chan 1984; Fiorino and Elsberry 1989; Elsberry 1995; Wu and Wang 2001b; Chan et al. 2002). This diabatic heating effect on TC
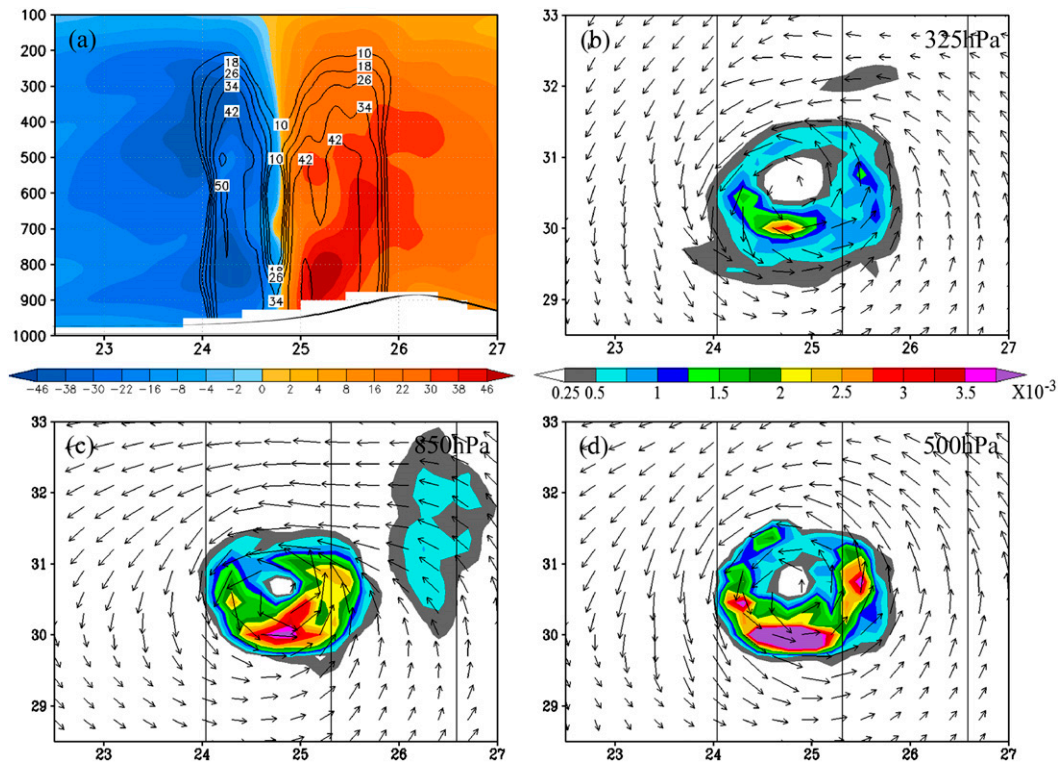
FIG. 12. For case CNTL, (a) east–west vertical section of the V (north–south) wind component (m s^{-1}; shaded) and radar echoes (dBZ; contours) across the TC center at 186 h. Distributions of total water content are shown for (b) 325, (c) 850, and (d) 500 hPa.

motion will be further elucidated in the next section. The zigzag track of the TC downstream of the mountain (e.g., the track for $x < 2000$ km in Fig. 2a) is attributed to the reorganization process of the TC, which tends to prohibit the TC moving along a smoother trajectory.

Note that the strong reduction of moisture in upper levels (e.g., Fig. 8l) tends to weaken the vertical coupling mechanism from deep convection, which may lead the upper- and lower-level TC vortices to become decoupled and drift separately (e.g., Wang and Holland 1996; Wu and Wang 2001a,b), especially under strong orographic blocking. This can ultimately lead to track discontinuity or even track looping. In addition, as discussed in the previous subsection, the northerly asymmetric flow steering effect on upstream track deflection (Wu et al. 2015), it does not seem to play a significant role upstream of the mountain since the southward deflection has started earlier than at 150 h and $x = 3000$ km while the TC is still symmetric (Figs. 3a and 7a).

Based on Wu and Emanuel (1993) [also see Elsberry (1995) and Fig. 9.30 of Lin (2007) for brief reviews], a TC tends to be steered by the ventilation flow to the left of the shear vector (i.e., deflected toward north in a westerly shear flow). To examine the vertical shear effect, the zonal wind u field is analyzed on the east–west vertical cross section passing through the center of the storm (Fig. 7). Far away from the mountain and the TC (e.g., $x > 3300$ km at 150 h), there exists no strong wind shear generated in the layer from near the surface to 250 hPa (Fig. 7a). At this time (150 h), the deep shear vector is pointing eastward (i.e., westerly shear vector), which would steer the TC to move northward, according to the theory of Wu and Emanuel (1993). This is opposite to the southward deflection at this hour. At later times (Figs. 7c,d), there is also no strong vertical shear of the zonal wind. Thus, it appears that the shear effect plays an insignificant role in the southward deflection for the present case.

4. Vorticity budget analysis

It is well established that a TC tends to move toward an area with a positive VT [e.g., see Holland (1983) and Elsberry (1995)]. This is also demonstrated in Fig. 2a for case CNTL. In this section, a vorticity budget analysis is conducted to help understand the major effects influencing TC track deflection. These include cyclonic circulation, mean flow advection, and latent heating. In
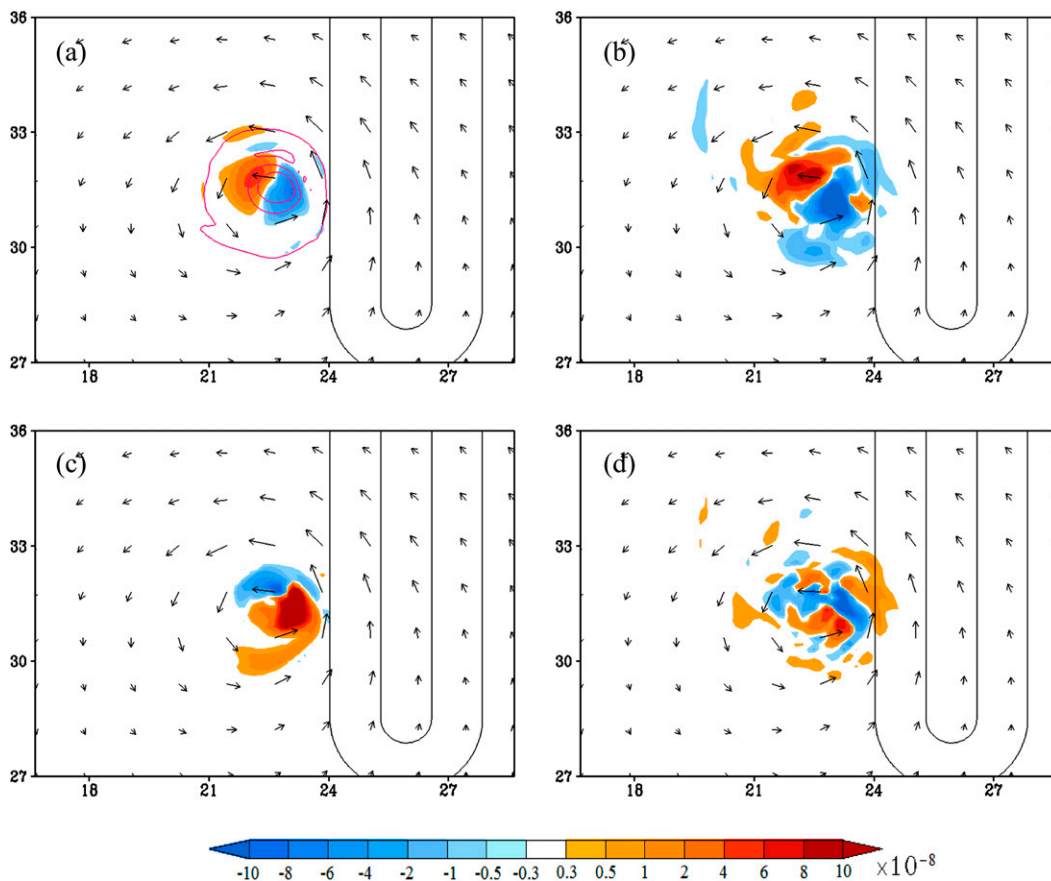
FIG. 13. As in Fig. 9, but for 207 h.

addition, the latent heating effect is further elucidated by conducting a vorticity budget analysis for a case with diabatic heating deactivated (i.e., NOHT).

The vorticity equation in sigma–pressure (σ–p) coordinates on an f plane may be written as

$$\underbrace{\frac{\partial \zeta}{\partial t}}_{1} = \underbrace{-\mathbf{V}_H \cdot \nabla \zeta}_{2} + \underbrace{\zeta \frac{\partial \omega}{\partial p}}_{3}$$
$$+ \underbrace{\left[-\omega \frac{\partial \zeta}{\partial p} + f_o \frac{\partial \omega}{\partial p} + \left(\frac{\partial \omega}{\partial y} \frac{\partial u}{\partial p} - \frac{\partial \omega}{\partial x} \frac{\partial v}{\partial p} \right) + F \right]}_{4},$$

$$(3)$$

where $\mathbf{V}_H$ is the horizontal wind vector (zonal u, meridional v), ω is the omega vertical motion, and f_o is the constant Coriolis parameter of 5×10^{-5} s^{-1}. In Eq. (3), terms 1–4 represent the VT, horizontal vorticity advection, vorticity stretching associated with relative vorticity, and the residual term, respectively. The residual term includes the vertical vorticity advection [$\omega(\partial \zeta / \partial p)$], vorticity stretching associated with planetary vorticity [$f_o(\partial \omega / \partial p)$], tilting term (the term containing $\partial u / \partial p$ and $\partial v / \partial p$), and

term F. Based on detailed comparisons, we found that the residual term is dominated by F, which cannot be ignored compared to terms 1–3. Note that term F includes friction, subgrid turbulence mixing, and numerical smoothing (diffusion), etc. It is difficult to isolate individual terms within term F. In fact, term F may also include latent heating effects via convection-induced turbulence mixing. In the vorticity analysis, the residual term (term 4) is calculated by subtracting terms 2 and 3 from VT (term 1).

Figure 9 shows the surface–500-hPa-layer-averaged VT, horizontal vorticity advection, vorticity stretching, and residual terms for case CNTL at 150 h when the TC is located upstream of the mountain. To avoid rapid temporal changes, these fields are averaged with those 3 h before and after 150 h, but with the center shifted to the same location of 150 h. The relative vorticity (Fig. 9a) and vector wind fields are also plotted for reference. Calculations are on the terrain-following pressure (σ–p) surfaces. At 150 h, the TC is located at $x = 3000$ km, about 400 km upstream of the mountain ridge line (Fig. 9a). As shown in Figs. 2a and 3a, at this time the TC has already started moving southwestward toward the area with maximum VT (Fig. 9a). This area of
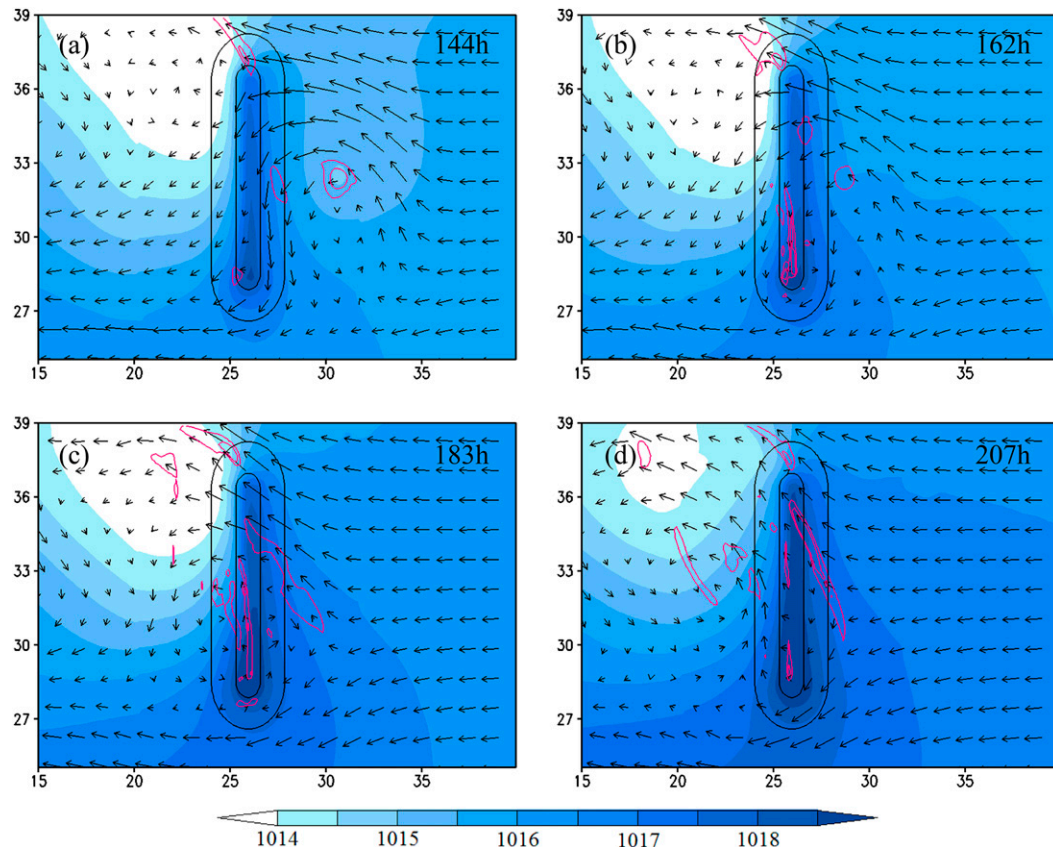
FIG. 14. For case NOHT, MSLP (shading), 850-hPa (σ surface) relative vorticity (contours in magenta), and vector wind fields at (a) 144, (b) 162, (c) 183, and (d) 207 h. The relative vorticity contours are 5×10^{-5}, 1×10^{-4}, 5×10^{-4}, 1×10^{-3}, 2×10^{-3}, and $3 \times 10^{-3}\,\mathrm{s}^{-1}$. The mountain height contours are 100 and 600 m.

positive VT is accompanied by an area of negative VT located to the northeast and is mainly contributed by the horizontal vorticity advection (Fig. 9b) with additional contributions from vorticity stretching (Fig. 9c) and the residual term (Fig. 9d). The southward advection is mainly associated with the subgeostrophic wind developed over the upslope (eastern slope) due to blocking, as depicted in Figs. 1b and 20 (Fig. 20 is described in greater detail below) and the relevant discussion. The area of negative vorticity advection centered at $(x, y) =$ (2900, 3100 km) is compensated by the positive vorticity stretching and residual terms. The vorticity stretching (Fig. 9c) is mainly contributed by the latent heating associated with eyewall convection, which can be seen from the rainfall pattern (Fig. 3a) and cloud or total water content patterns (Figs. 8a–c). The residual term (Fig. 9d) has three maxima surrounding the eyewall convection, which may be caused by complicated PBL friction, subgrid turbulent mixing, and numerical diffusion, etc., with one in particular located to the southwest of the TC center contributing to the positive VT at this time. Thus, the southwestward track deflection upstream

of the mountain is mainly contributed by the vorticity advection with additional contributions from the vorticity stretching and residual terms.

Figure 10 shows the vorticity budget analysis similar to Fig. 9 except at 171 h when the TC is over the upslope (Fig. 3b). Similar to that at 150 h, the VT field shows a positive VT area located to the west-southwest of the TC vortex center, accompanied by a negative VT area to the east-northeast (Fig. 10a). The positive VT is contributed by all horizontal vorticity advection (Fig. 10b), vorticity stretching (Fig. 10c), and residual (Fig. 10d) terms. The pattern of the residual term is more complicated (Fig. 10d) than that at 150 h (Fig. 9d); however, it has an organized, broad area of positive areas at and to the west-southwest of the TC center. Thus, when the TC moves to the upslope, all horizontal vorticity advection, vorticity stretching, and residual terms have contributed to the maximum positive VT. Figure 11 shows the vorticity budget analysis at 186 h when the TC is over the lee slope (Fig. 3c). At this time, the maximum VT is shifted to the northwest of the TC center (Fig. 11a). Thus, the TC is steered northwestward, which is consistent with
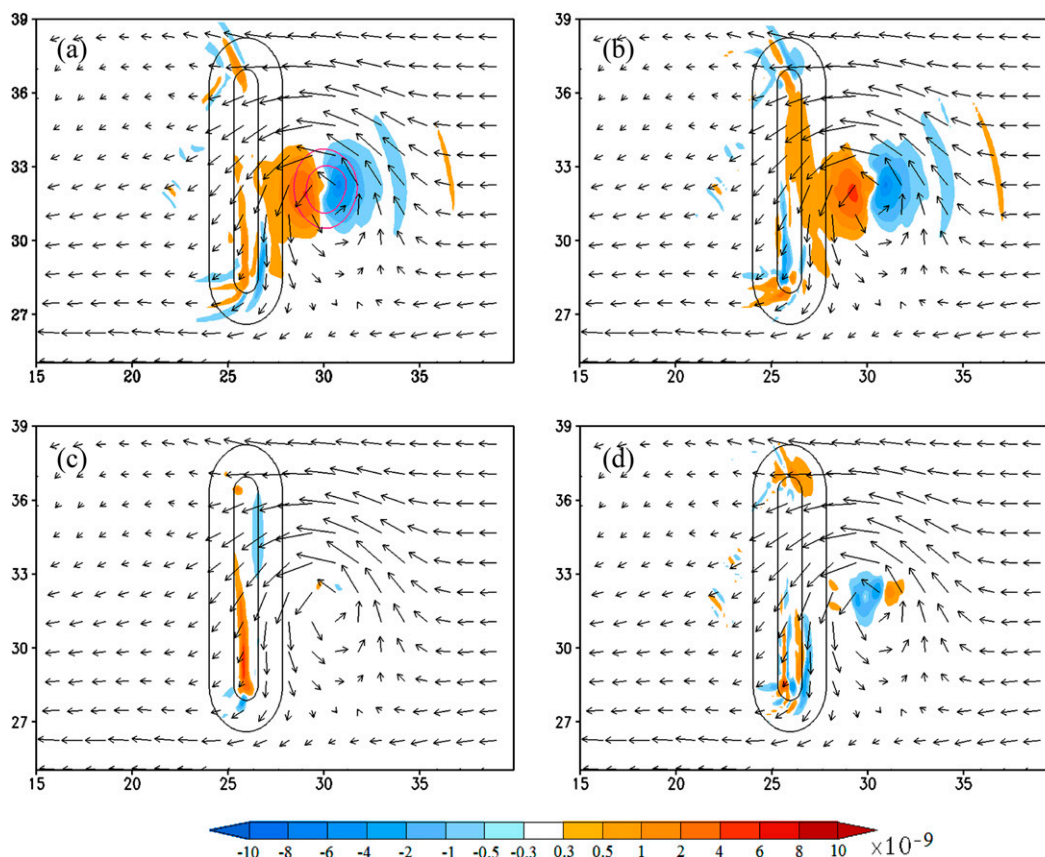
FIG. 15. For case NOHT, the surface–500-hPa-layer-averaged vector wind field and (a) VT and relative vorticity (contours in magenta), (b) horizontal vorticity advection, (c) vorticity stretching, and (d) residual term at 144 h. The averaged-layer relative vorticity contours in (a) are 5×10^{-5}, 1×10^{-4}, 5×10^{-4}, 1×10^{-3}, 2×10^{-3}, and $5 \times 10^{-3}\,\mathrm{s}^{-1}$.

the simulated TC track (Fig. 2). Similar to that over the upslope (Fig. 10), the maximum VT located to the northwest of the TC center is mainly contributed by the horizontal vorticity advection (Fig. 11b) with additional contributions from the vorticity stretching (Fig. 11c) and the residual term (Fig. 11d). The northwestward advection is associated with the anticyclonic flow due to orographically generated high pressure in response to the basic flow over mountains (also see Fig. 20, described in greater detail below, and the relevant discussion).

Note that the asymmetric vorticity stretching (Fig. 11c), with its maximum located to the southeast of the TC center, reflects the latent heat associated with the asymmetric eyewall convection (Figs. 3c and 8g–i). The asymmetric eyewall convection is clearly shown in the zoomed-in radar echoes with a stronger convection on the eastern flank (Fig. 12a). With stronger northward wind component, the self-induced storm advection associated with the asymmetric diabatic heating mechanism enhances the northwestward movement discussed above. The distributions of total water content,

especially in the lower and midtroposphere (Figs. 12c,d), also support the proposed mechanism.

Figure 13 shows the vorticity budget analysis similar to Fig. 9 except at 207 h when the TC moves downstream of the mountain. The maximum VT, which is located to the northwest of the TC center (Fig. 13a), is primarily dominated by the horizontal vorticity advection (Fig. 13b). Note that the TC convection has been disrupted significantly by the mountain and has become very asymmetric, with much stronger eyewall convection to the east (Figs. 3d and 7d). The contribution of this asymmetric diabatic heating effect on the storm motion, as discussed in section 3b, is through the generation of latent heating near $(x, y) = (2300, 3150\,\mathrm{km})$ (Figs. 3d, 7d, and 13c) and the northward advection of convective clouds (Figs. 8j–l) by the local wind (Fig. 13b). This helps explain the more abrupt northwestward movement, compared to the smoother southwestward movement upstream of the mountain (Fig. 2). Note, this effect will not occur if the diabatic heating or PV is symmetric since the advection of PV by the vortex circulation will be azimuthal.
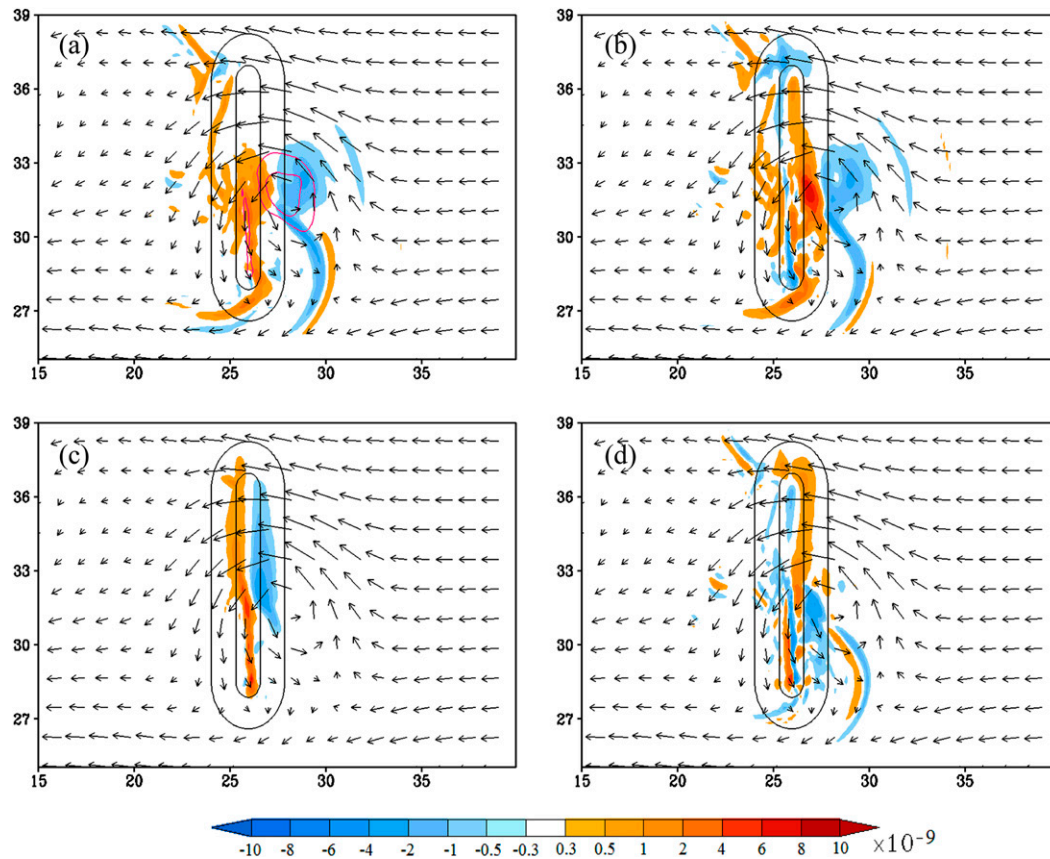
FIG. 16. As in Fig. 15, but for 162 h.

To further elucidate the latent heating effect on track deflection, we perform a simulation with diabatic heating deactivated (i.e., NOHT) and conduct a vorticity budget analysis. Without latent heating, the dry vortex is much weaker upstream of the mountain (Figs. 14a and 3a). In addition, the vortex is difficult to track when it is passing over the mountain owing to influences from the orography and orographically generated lee cyclone (Figs. 14b–d). The budget analysis of NOHT (Figs. 15–18) clearly indicates that the VT is dominated by the horizontal vorticity advection, consistent with that found in Lin and Savage (2011) for a vortex over a mountain in a dry flow. The positive (negative) vorticity stretching (shrinking) is associated with the basic flow (Fig. 15c) or TC outer circulation (Figs. 16c and 17c) going downslope (upslope). This suggests vorticity stretching in a dry flow only affects the track deflection when the TC is passing over the mountain. The residual term, which mainly represents the effects of friction and subgrid turbulence mixing, is less organized and, as a result, makes no significant contribution to the track deflection.

In the cyclonic circulation effect proposed by Chang (1982), the cumulus heating in the vicinity of the mountain may generate and maintain a cyclonic circulation around the topography, which then helps steer the low-level storm center to pass over the mountain cyclonically. Based on the above analysis, the latent heating does help sustain the TC convection when the storm passes over the mountain. However, there is no apparent evidence supporting this mechanism. Instead, the storm passes over the mountain anticyclonically (Fig. 2). Thus, the cyclonic circulation effect is not applicable to the present case; however, it may be applicable to an environment with weaker blocking, such as for a larger TC or a shorter mountain range (e.g., L05).

In summary, the TC movement closely follows the maximum VT. Positive VT is dominated by the horizontal vorticity advection upstream and downstream of the mountain but is also contributed by the vorticity stretching (diabatic heating) and residual term (friction, subgrid turbulent mixing, and other effects) when the TC is passing over the mountain. The latent heating helps sustain the TC while it passes over the mountain, as revealed by the comparison of moist (i.e., CNTL) and dry (i.e., NOHT) cases, but the cyclonic circulation mechanism is not applicable to the present case. The
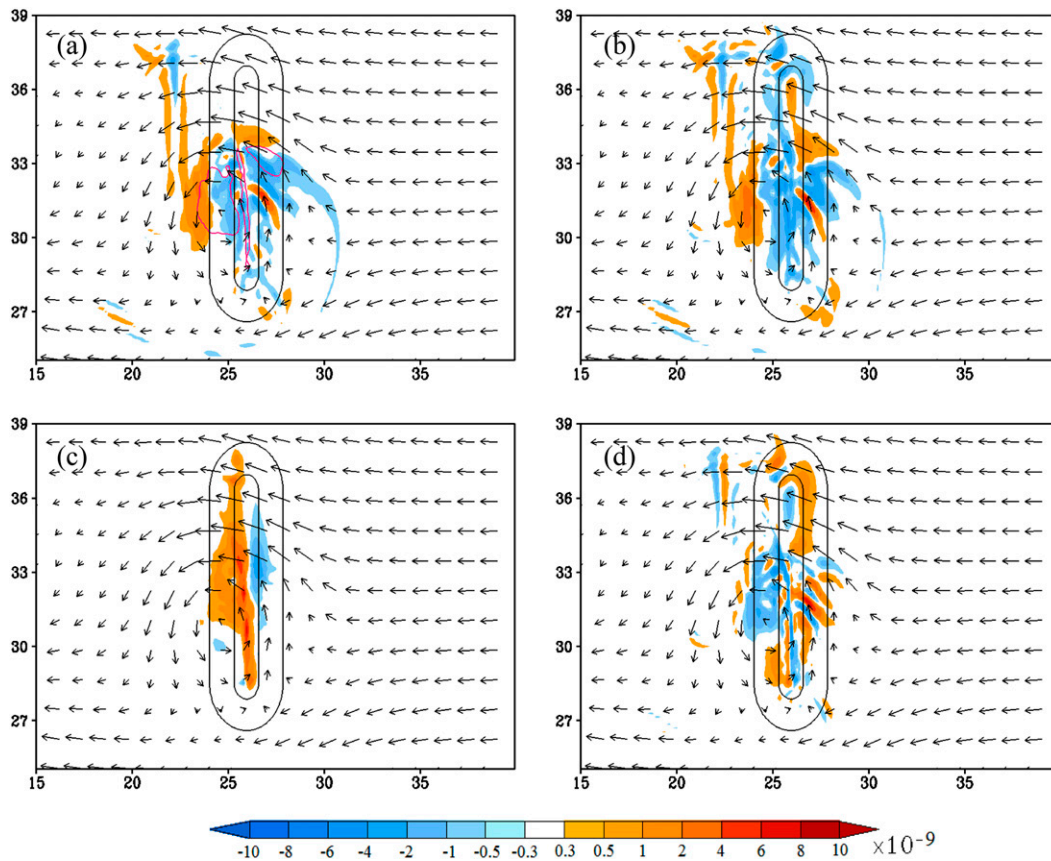
FIG. 17. As in Fig. 15, but for 183 h.

asymmetric diabatic heating downstream of the mountain is found to be associated with a positive vorticity advection, which helps explain the abrupt northwestward movement of the TC after passing over the mountain. There is no apparent evidence supporting effects of asymmetric flow steering and cyclonic circulation on track deflection in the present case, although this does not exclude that they may play more significant roles under different flow and/or orographic settings.

5. Upstream orographic influence on the basic flow and TC movement

In this section, the upstream orographic influence on the basic flow and TC movement and its relation to the channeling and the latent heating effects is investigated. Based on the vorticity budget analysis of the numerically simulated idealized TC over an idealized mountain range performed (i.e., CNTL) in the previous section, we hypothesize that when a TC approaches the mountain, it is advected or steered by the deep-layer environmental flow, as depicted in Fig. 1b, analogous to the advection of a point vortex in a flow. To verify this

hypothesis, we performed a numerical experiment identical to CNTL but with no TC (i.e., NOTC).

Figure 19 shows the perturbation geopotential height on the 950-hPa σ surface where the easterly basic flow is blocked and split upstream of the mountain. This produces a perturbation high pressure over the mountain inducing anticyclonic flow, as found in dry mountain wave theories [e.g., see Smith (1979) and chapter 5 of Lin (2007) for reviews]. The flow near the central portion of the mountain is also similar to that depicted in Fig. 1b for a stratified, uniform fluid flow over an infinitely long mountain, which turns northeasterly near the mountain. The stagnation point generated by the orographic blocking is located to the north of the centerline ($y_0 = 3255$ km). For case NOTC, the basic-flow Froude number is approximately 0.5, indicating a moderate blocking on the basic flow. The orographic blocking tends to reduce the moving speeds of the TC to 3.66 and 4.85 m s^{-1} for cases CNTL (Fig. 3) and NOMT (Fig. 4), respectively. Thus, for a TC vortex moving along the central line far upstream, it tends to be advected to the south by the orographically deflected northeasterly basic wind, analogous to the advection of a
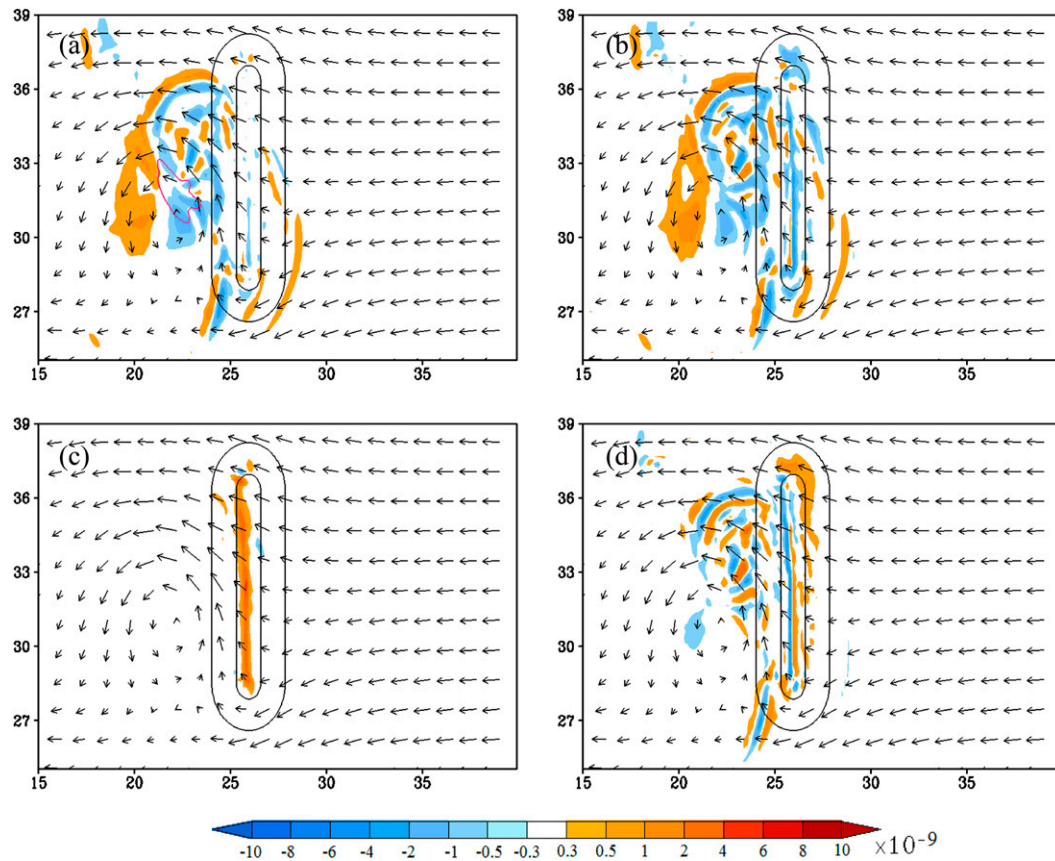
FIG. 18. As in Fig. 15, but for 207 h.

point vortex in a flow. This argument is also consistent with the findings of Lin et al. (1999) and L05, where the direction of track deflection (north or south for a westward-moving vortex) is determined more by the basic-flow Froude number, while the degree of track deflection is determined more by the vortex Froude number (i.e., V_{max}/Nh). Note that when a TC approaches the northern portion of the mountain, it tends to be advected to the north by the basic flow (e.g., Lin and Savage 2011; Liu et al. 2016).

In the channeling effect (Lin et al. 1999; Jian and Wu 2008; Huang et al. 2011), the southward deflection of the TC upstream of the mountain is attributed to the advection of the TC vortex by the northerly jet produced by the orographic blocking, basic flow, and TC outer circulation. A close inspection of Fig. 3a (CNTL) and Fig. 18 (NOHT) reveals that a stronger low-level northerly flow is indeed induced near the channel formed between the mountain and the TC outer circulation. The north–south wind component and surface–500-hPa-layer-averaged flow field (Fig. 20) is similar to Fig. 19 except that the disturbance is weaker owing to much smaller flow deflection in upper levels. The

stagnation point is located at about $y_0 = 3400$ km, and the flow on the lee side is less curvy, implying a shallow orographically generated lee vortex. Since this northerly flow is not strong enough to be called a northerly jet, similar to that found in Wu et al. (2015), the channeling effect does not seem to be playing a role in the present case. In addition, there exists no vorticity advection in between the TC and the mountain (Fig. 9b).

The mean flow advection effect is further investigated by tracking a circular passive tracer, which is composed of a circular chain of air parcels and released at the same column as the TC initial position in CNTL ($t = 0$ h). Figure 21 shows the locations and distributions of these passive tracers at 850, 500, and 325 hPa upstream of the mountain (132 h), upslope (147 h), lee slope (165 h), and downstream of the mountain (180 h). It is clear that the circular tracer at the lowest level (850 hPa) is deflected to the south upstream of the mountain (Fig. 21a) and over the upslope (Fig. 21b), but then moves northward over the lee slope, and then resumes its westward movement downstream of the mountain. Similar to case NOTC (Figs. 19 and 20), the deflection of the tracer is
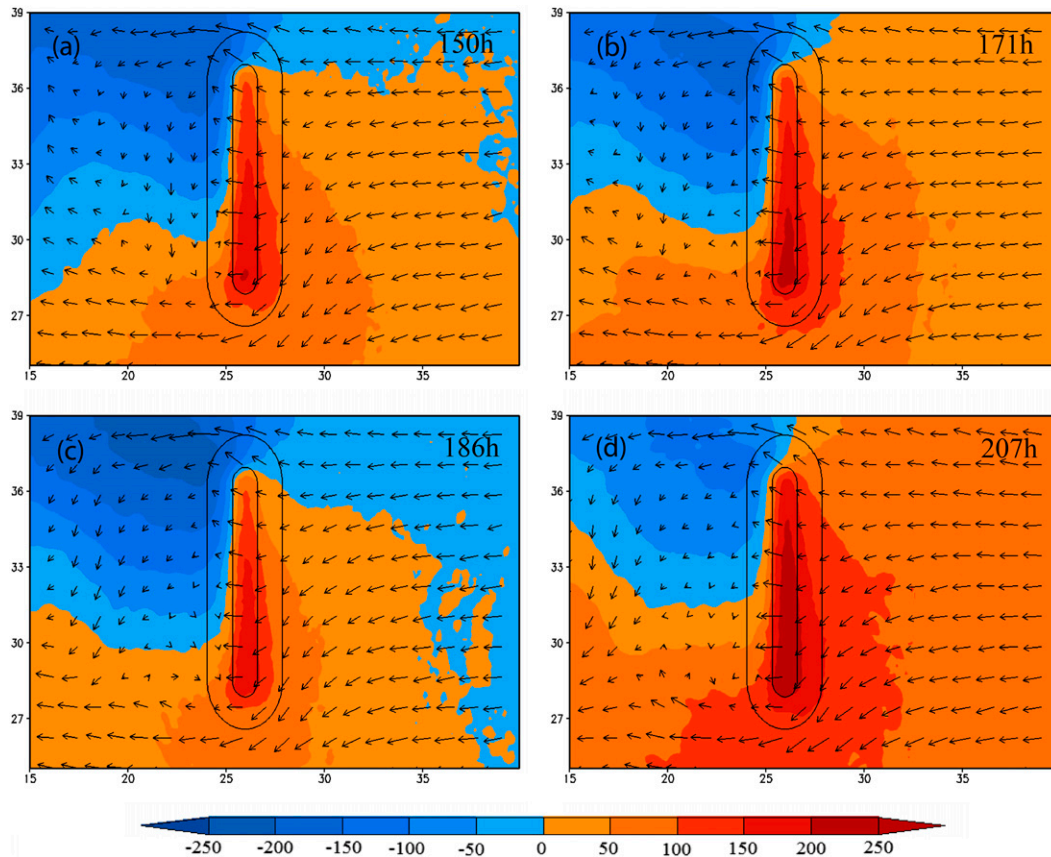
FIG. 19. For case NOTC, the 950-hPa (σ surface) perturbation geopotential height (m; color shaded) and wind vector fields at (a) 150, (b) 171, (c) 186, and (d) 207 h.

more pronounced in the lower levels than in the upper levels. In addition, its pattern is severely distorted and, compared to the upper-level trackers, it moves downstream the slowest because of orographic blocking and surface friction. In other words, Fig. 21 shows that the orographically deflected easterly basic wind is able to advect the air parcels southward upstream of the mountain. The TC track would behave like the passive tracer except that the latent heating tends to help the deflected TC at lower levels develop upward and maintain its vertical coherent structure as simulated in case CNTL (Fig. 8). Here, a slight phase difference in the vertical can still be seen, though not as pronounced as those in the passive tracer.

In case NOHT, both the surface–500-hPa maximum relative vorticity and maximum VT of the dry TC vortex start to move southward as far as 800 km upstream of the mountain ($x \approx 3400$ km) (Fig. 22). This southward track deflection upstream of the mountain can be explained by the steering of the orographically influenced basic flow, analogous to the advection of a point vortex. Note that the vortex is difficult to track

when it reaches the upslope of the mountain. For this reason, the track is not plotted over and downstream of the mountain.

6. Concluding remarks

In this study, a series of idealized numerical experiments is performed to examine several mechanisms proposed in previous studies using ARW to help understand the orographic influence on TC track deflection over a mesoscale mountain range. These mechanisms include mean flow advection, cyclonic circulation, channeling, asymmetric flow steering, asymmetric latent heating, and vertical shear effects by conducting a series of experiments.

When an idealized TC is embedded in a uniform, easterly flow over a mesoscale mountain with a moderate Froude number (e.g., 0.5), it is deflected to the south upstream of the mountain, crosses over the mountain anticyclonically as a result of the orographically induced high pressure, and then resumes its westward movement downstream of the mountain. The track continuity is consistent with the moderate blocking regime proposed
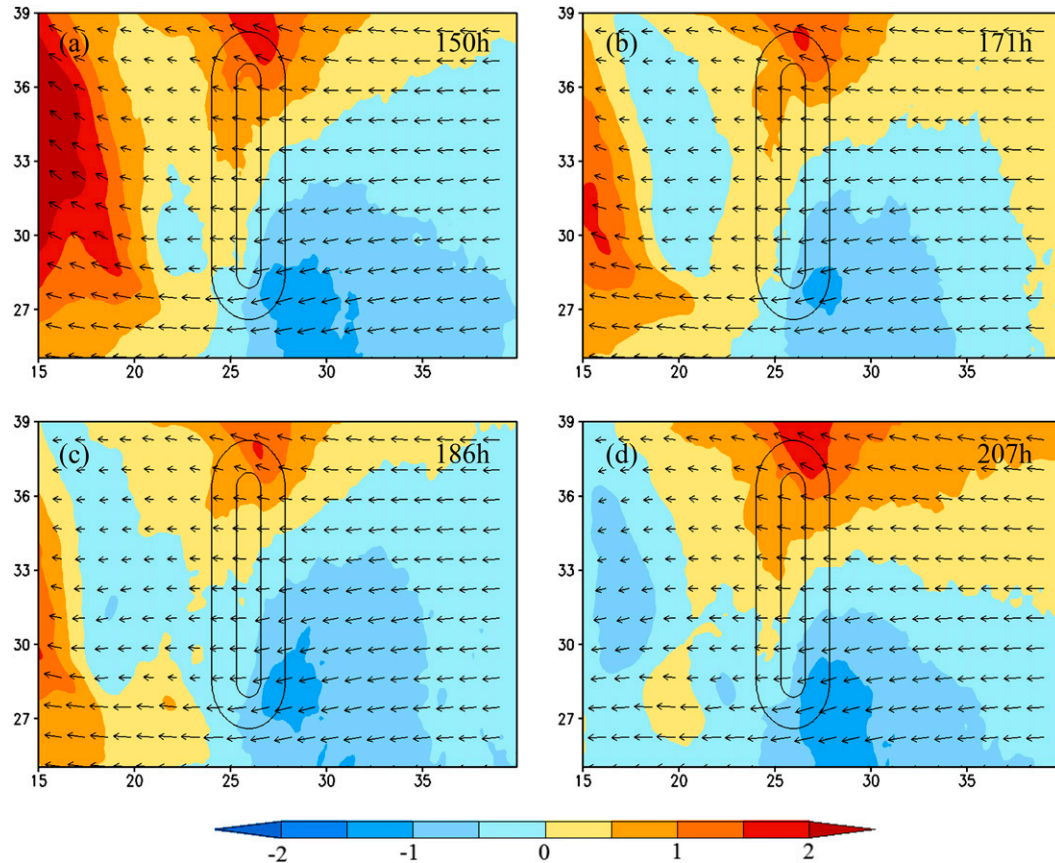
FIG. 20. For case NOTC, the surface–500-hPa-layer-averaged V (north–south) wind component and wind vector fields at (a) 150, (b) 171, (c) 186, and (d) 207 h. The V wind is shaded in yellow or red for $V > 0$ (with southerly wind component) and blue for $V < 0$ (with northerly wind component).

in L05. The accumulated rainfall accompanying the TC shows a path almost identical to the TC-track-following lower-level minimum pressure center and VT. Before reaching the upslope of the mountain, the TC is able to retain its symmetry in MSLP, rainfall, and total wind patterns. As a result of the upstream orographic influence, the southward deflection of the TC starts as far as 700 km before the mountain peak.

The asymmetric flow steering effect (Wu et al. 2015) does not seem to play a major role on track deflection in the present case since there is no apparent northerly asymmetric flow found upstream of the mountain. It should be noted that this does not rule out its potential role in upstream TC deflection under different flow, mountain, and TC settings. When the TC moves over the upslope, the western flank of the eyewall convection is severely weakened by orographic blocking, as evidenced in the accompanied rainfall pattern. In addition, the storm asymmetry is also partially caused by the natural evolution of the TC intensity, as revealed in the evolutions of P_{min} and ζ_{max} in case CNTL and the rainfall

pattern in case NOMT. Another significant orographic influence on the TC is the reduction of the zonal moving speed due to orographic blocking, which is about $3.66 \, \mathrm{m \, s^{-1}}$ for case CNTL versus $4.85 \, \mathrm{m \, s^{-1}}$ for case NOMT. A slightly southward movement in case CNTL is attributed to the blocking effect on the easterly basic flow resulting in a subgeostrophic flow. The eyewall becomes asymmetric over the upslope as the eastern flank of the eyewall deepens and intensifies, resulting in maximum rainfall over the eastern half of the storm. The western flank of the eyewall is significantly weakened by the mountain after the TC passes over the peak and becomes very weak and shallow farther downstream of the mountain.

Over the lee slope, the TC moves northwestward, as steered by the orographically induced high pressure. This northwestward movement is enhanced by the advection of the eyewall convective clouds associated with asymmetric diabatic heating and contributes to a more abrupt turning toward northwest, as revealed by the vorticity advection field. This self-induced advection
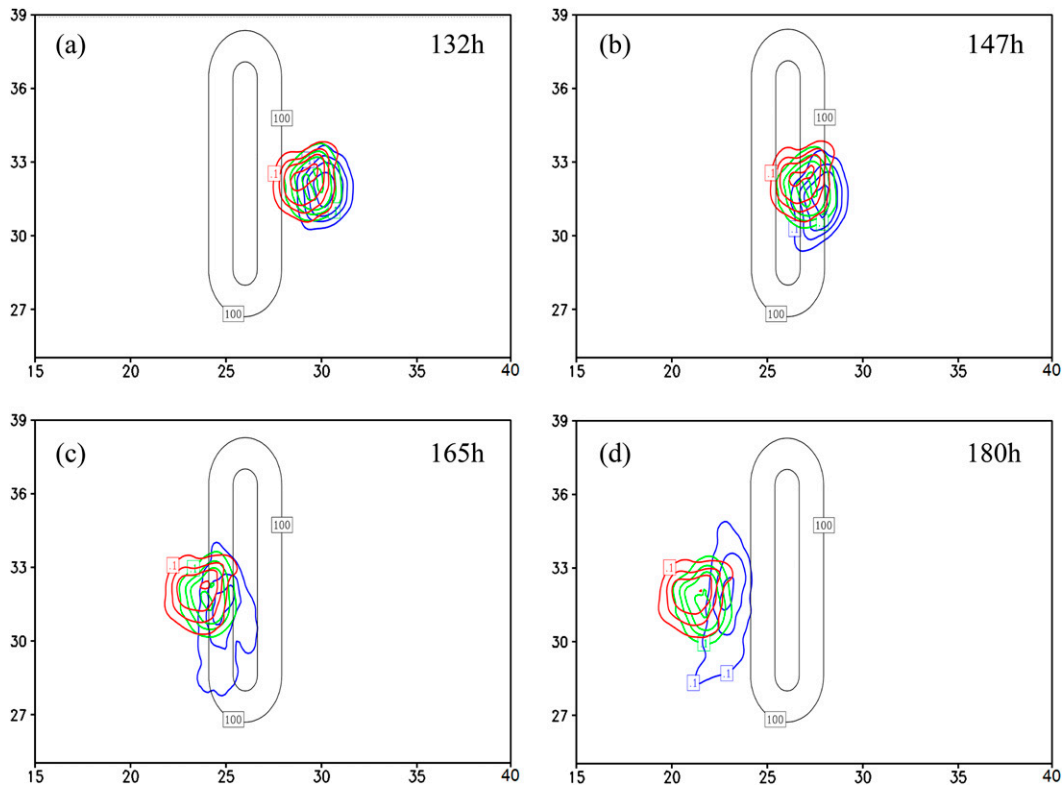
FIG. 21. For case NOTC, evolutions of three passive tracers on 850 (blue), 500 (green), and 325 (red) hPa surfaces. The tracer is a virtual circular chain of air parcels with a diameter of about 300 km. They are released at $t = 0$ h—that is, the same time as the initial bogus vortex is inserted in case CNTL with the centers located at $x = 5400$ km on 850, 500, and 325 hPa.

associated with asymmetric diabatic heating has been found in previous studies and where it is used to explain track deflection on the lee side of mountains. In addition, applying a theory of the shear effect on storm motion in the present case indicates that the shear effect plays an insignificant role in steering the southward deflection of the TC. The TC motion may be more sensitive to the shear associated with environmental flow. In addition, the lower-level TC vortex is deflected farther to the south (north) over the upslope (lee slope) compared to the upper-level TC vortex but remains phase locked in vertical with a slight phase tilt. When orographic blocking becomes strong, the upper- and lower-level TC vortices may decouple owing to differential vorticity advection and lead to a track discontinuity or even track looping. This hypothesis requires further verification in future studies.

Based on vorticity budget analyses, we find the following: 1) The TC movement can be predicted by the maximum vorticity tendency (VT). 2) Far upstream and downstream, the VT is primarily dominated by the horizontal vorticity advection. 3) Over the mountain, the VT is mainly contributed by the horizontal vorticity

advection with additional contributions from vorticity stretching and the residual term. 4) Over the lee slope and downstream of the mountain, the northward movement is enhanced by asymmetric diabatic heating, which also contributes to a more abrupt turning toward northwest. Note that the vorticity stretching is mainly associated with diabatic heating, while the residual term includes friction, subgrid turbulence mixing, and other effects. Based on
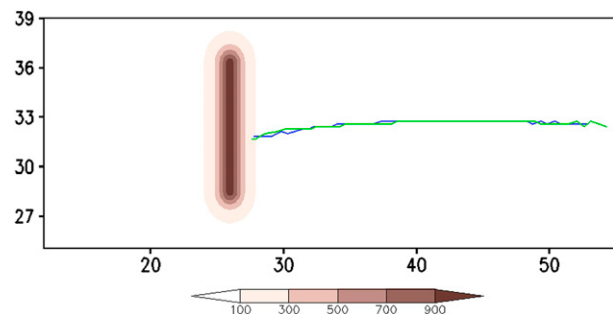

FIG. 22. For case NOHT, the tracks of surface–500-hPa max relative vorticity (green) and max VT (blue) of the dry TC vortex. Shading is the terrain height.

the vorticity budget analyses of case CNTL and the no latent heat (i.e., NOHT) case, the latent heating does help sustain the TC convection over the mountain, but there is no apparent evidence supporting a cyclonic circulation surrounding the mountain to steer the TC cyclonically over the mountain, as proposed by Chang (1982). Thus, the cyclonic circulation effect is not applicable to the present case, although it may be applicable to an environment with weaker blocking, such as for a larger TC or a shorter mountain range. The hypothesis of upstream deflection of a TC being advected or steered by the deep-layer environmental flow, analogous to a point vortex advection in a flow, is verified by analyzing the results of no TC (i.e., NOTC) versus CNTL. In addition, there is no strong evidence supporting the channeling effect.

Note that further studies are needed to more completely understand the orographic influence on TC tracks, such as the channeling effect on asymmetric TC structure upstream of the mountain, asymmetric flow developed upstream under different environmental settings (e.g., stronger blocking or asymmetric incoming TC), vertical shear associated with environmental flow, effects of asymmetric diabatic latent heating over upslope, effect of differential advection on possible track discontinuity and upstream track looping, etc., under various flow and orographic settings.

REFERENCES

Bender, M. A., R. E. Tuleya, and Y. Kurihara, 1987: A numerical study of the effect of an island terrain on tropical cyclones. *Mon. Wea. Rev.*, **115**, 130–155, doi:10.1175/1520-0493(1987)115<0130:ANSOTE>2.0.CO;2.

Brand, S., and J. W. Blelloch, 1974: Changes in the characteristics of typhoons crossing the island of Taiwan. *Mon. Wea. Rev.*, **102**, 708–713, doi:10.1175/1520-0493(1974)102<0708:CITCOT>2.0.CO;2.

Chan, J. C.-L., 1984: An observational study on the physical processes responsible for tropical cyclone motion. *J. Atmos. Sci.*, **41**, 1036–1048, doi:10.1175/1520-0469(1984)041<1036:AOSOTP>2.0.CO;2.

——, F. M. F. Ko, and Y. M. Lei, 2002: Relationship between potential vorticity tendency and tropical cyclone motion. *J. Atmos. Sci.*, **59**, 1317–1336, doi:10.1175/1520-0469(2002)059<1317:RBPVTA>2.0.CO;2.

Chang, S. W.-J., 1982: The orographic effects induced by an island mountain range on propagating tropical cyclones. *Mon. Wea. Rev.*, **110**, 1255–1270, doi:10.1175/1520-0493(1982)110<1255:TOEIBA>2.0.CO;2.

Chen, S.-H., and W.-Y. Sun, 2002: A one-dimensional time-dependent cloud model. *J. Meteor. Soc. Japan*, **80**, 99–118, doi:10.2151/jmsj.80.99.

——, and Y.-L. Lin, 2005: Effects of the basic wind speed and CAPE on flow regimes associated with a conditionally unstable flow over a mesoscale mountain. *J. Atmos. Sci.*, **62**, 331–350, doi:10.1175/JAS-3380.1.

Dunion, J. P., 2011: Rewriting the climatology of the tropical North Atlantic and Caribbean Sea atmosphere. *J. Climate*, **24**, 893–908, doi:10.1175/2010JCLI3496.1.

Elsberry, R. L., Ed., 1995: Global perspective of tropical cyclones. WMO Tech. Doc. WMO/TD-693, 289 pp.

Emanuel, K. A., 1994: *Atmospheric Convection.* Oxford University Press, 580 pp.

Fiorino, M., and R. L. Elsberry, 1989: Some aspects of vortex structure related to tropical cyclone motion. *J. Atmos. Sci.*, **46**, 975–990, doi:10.1175/1520-0469(1989)046<0975:SAOVSR>2.0.CO;2.

Harville, S. L., 2009: Effects of Appalachian topography on precipitation from landfalling hurricanes. M.S. thesis, North Carolina State University, 320 pp. [Available online at http://repository.lib.ncsu.edu/ir/handle/1840.16/2849.]

Holland, G. J., 1983: Tropical cyclone motion: Environmental interaction plus a beta-effect. *J. Atmos. Sci.*, **40**, 328–342, doi:10.1175/1520-0469(1983)040<0328:TCMEIP>2.0.CO;2.

Hong, S.-Y., and H.-L. Pan, 1996: Nonlocal boundary layer vertical diffusion in a Medium-Range Forecast Model. *Mon. Wea. Rev.*, **124**, 2322–2339, doi:10.1175/1520-0493(1996)124<2322:NBLVDI>2.0.CO;2.

Hsu, L.-H., H.-C. Kuo, and R. G. Fovell, 2013: On the geographic asymmetry of typhoon translation speed across the mountainous island of Taiwan. *J. Atmos. Sci.*, **70**, 1006–1022, doi:10.1175/JAS-D-12-0173.1.

Huang, Y.-H., C.-C. Wu, and Y. Wang, 2011: The influence of island topography on typhoon track deflection. *Mon. Wea. Rev.*, **139**, 1708–1727, doi:10.1175/2011MWR3560.1.

Jian, G.-J., and C.-C. Wu, 2008: A numerical study of the track deflection of Supertyphoon Haitang (2005) prior to its landfall in Taiwan. *Mon. Wea. Rev.*, **136**, 598–615, doi:10.1175/2007MWR2134.1.

Kain, J. S., 2004: The Kain–Fritsch convective parameterization: An update. *J. Appl. Meteor.*, **43**, 170–181, doi:10.1175/1520-0450(2004)043<0170:TKCPAU>2.0.CO;2.

——, and J. M. Fritsch, 1993: Convective parameterization for mesoscale models: The Kain–Fritsch scheme. *The Representation of Cumulus Convection in Numerical Models, Meteor. Monogr.*, No. 46, Amer. Meteor. Soc., 165–170.

Lin, Y.-L., 2007: *Mesoscale Dynamics.* Cambridge University Press, 630 pp.

——, and L. C. Savage III, 2011: Effects of landfall location and the approach angle of a cyclone vortex encountering a mesoscale mountain range. *J. Atmos. Sci.*, **68**, 2095–2106, doi:10.1175/2011JAS3720.1.

——, R. D. Farley, and H. D. Orville, 1983: Bulk parameterization of the snow field in a cloud model. *J. Climate Appl. Meteor.*, **22**, 1065–1092, doi:10.1175/1520-0450(1983)022<1065:BPOTSF>2.0.CO;2.

——, J. Han, D. W. Hamilton, and C.-Y. Huang, 1999: Orographic influence on a drifting cyclone. *J. Atmos. Sci.*, **56**, 534–562, doi:10.1175/1520-0469(1999)056<0534:OIOADC>2.0.CO;2.

——, S.-Y. Chen, C. M. Hill, and C.-Y. Huang, 2005: Control parameters for tropical cyclones passing over mesoscale mountains. *J. Atmos. Sci.*, **62**, 1849–1866, doi:10.1175/JAS3439.1.

——, N. C. Witcraft, and Y.-H. Kuo, 2006: Dynamics of track deflection associated with the passage of tropical cyclones over a mesoscale mountain. *Mon. Wea. Rev.*, **134**, 3509–3538, doi:10.1175/MWR3263.1.

Liu, L., Y.-L. Lin, and S.-H. Chen, 2016: Effects of landfall location and approach angle of an idealized tropical cyclone over a long mountain range. *Front. Earth Sci.*, **4**, 14, doi:10.3389/feart.2016.00014.

Mallen, K. J., M. T. Montgomery, and B. Wang, 2005: Reexamining the near-core radial structure of the tropical cyclone primary circulation: Implications for vortex resiliency. *J. Atmos. Sci.*, **62**, 408–425, doi:10.1175/JAS-3377.1.

Monin, A. S., and A. M. Obukhov, 1954: Basic laws of turbulent mixing in the surface layer of the atmosphere (in Russian). *Contrib. Geophys. Inst. Acad. Sci. USSR*, **151**, 163–187.

Nolan, D. S., 2011: Evaluating environmental favorableness for tropical cyclone development with the method of point-downscaling. *J. Adv. Model. Earth Syst.*, **3**, M08001, doi:10.1029/2011MS000063.

——, R. Atlas, K. T. Bhatia, and L. R. Bucci, 2013: Development and validation of a hurricane nature run using the joint OSSE nature run and the WRF Model. *J. Adv. Model. Earth Syst.*, **5**, 382–405, doi:10.1002/jame.20031.

Pierrehumbert, R. T., and B. Wyman, 1985: Upstream effects of mesoscale mountains. *J. Atmos. Sci.*, **42**, 977–1003, doi:10.1175/1520-0469(1985)042<0977:UEOMM>2.0.CO;2.

Rostom, R., and Y.-L. Lin, 2015: Control parameters for track continuity of cyclones passing over the south-central Appalachian Mountains. *Wea. Forecasting*, **30**, 1429–1449, doi:10.1175/WAF-D-14-00080.1.

Rutledge, S. A., and P. V. Hobbs, 1984: The mesoscale and microscale structure and organization of clouds and precipitation in midlatitude clouds. XII: A diagnostic modeling study of precipitation development in narrow cold-frontal rainbands. *J. Atmos. Sci.*, **41**, 2949–2972, doi:10.1175/1520-0469(1984)041<2949:TMAMSA>2.0.CO;2.

Skamarock, W. C., and Coauthors, 2008: A description of the Advanced Research WRF version 3. NCAR Tech. Note NCAR/TN-475+STR, 113 pp., doi:10.5065/D68S4MVH.

Smith, R. B., 1979: The influence of mountains on the atmosphere. *Advances in Geophysics*, Vol. 21, Academic Press, 87–230.

Smith, R. K., and G. L. Thomsen, 2010: Dependence of tropical-cyclone intensification on the boundary-layer representation in a numerical model. *Quart. J. Roy. Meteor. Soc.*, **136**, 1671–185, doi:10.1002/qj.687.

Tang, C. K., and J. C. L. Chan, 2014: Idealized simulations of the effect of Taiwan and Philippines topographies on tropical cyclone tracks. *Quart. J. Roy. Meteor. Soc.*, **140**, 1578–1589, doi:10.1002/qj.2240.

——, and ——, 2015: Idealized simulations of the effect of local and remote topographies on tropical cyclone tracks. *Quart. J. Roy. Meteor. Soc.*, **141**, 2045–2056, doi:10.1002/qj.2498.

Tewari, M., and Coauthors, 2004: Implementation and verification of the unified NOAH land surface model in the WRF Model. *20th Conf. on Weather Analysis and Forecasting/16th Conf. on Numerical Weather Prediction*, Seattle, WA, Amer. Meteor. Soc., 14.2a. [Available online at https://ams.confex.com/ams/84Annual/techprogram/paper_69061.htm.]

Wang, C.-C., H.-C. Kuo, Y.-H. Chen, H.-L. Huang, C.-H. Chung, and K. Tsuboki, 2012: Effects of asymmetric latent heating on typhoon movement crossing Taiwan: The case of Morakot (2009) with extreme rainfall. *J. Atmos. Sci.*, **69**, 3172–3196, doi:10.1175/JAS-D-11-0346.1.

——, Y.-H. Chen, H.-C. Kuo, and S.-Y. Huang, 2013: Sensitivity of typhoon track to asymmetric latent heating/rainfall induced by Taiwan topography: A numerical study of Typhoon Fanapi (2010). *J. Geophys. Res. Atmos.*, **118**, 3292–3308, doi:10.1002/jgrd.50351.

Wang, S.-T., 1980: Prediction of the movement and strength of typhoons in Taiwan and its vicinity. National Science Council Research Rep. 108, 100 pp.

Wang, Y., and G. J. Holland, 1996: Tropical cyclone motion and evolution in vertical shear. *J. Atmos. Sci.*, **53**, 3313–3332, doi:10.1175/1520-0469(1996)053<3313:TCMAEI>2.0.CO;2.

Wu, C.-C., 2001: Numerical simulation of Typhoon Gladys (1994) and its interaction with Taiwan terrain using the GFDL hurricane model. *Mon. Wea. Rev.*, **129**, 1533–1549, doi:10.1175/1520-0493(2001)129<1533:NSOTGA>2.0.CO;2.

——, and K. A. Emanuel, 1993: Interaction of a baroclinic vortex with background shear: Application to hurricane movement. *J. Atmos. Sci.*, **50**, 62–76, doi:10.1175/1520-0469(1993)050<0062:IOABVW>2.0.CO;2.

——, T.-H. Li, and Y.-H. Huang, 2015: Influence of mesoscale topography on tropical cyclone tracks: Further examination of the channeling effect. *J. Atmos. Sci.*, **72**, 3032–3050, doi:10.1175/JAS-D-14-0168.1.

Wu, L., and B. Wang, 2001a: Movement and vertical coupling of adiabatic baroclinic tropical cyclones. *J. Atmos. Sci.*, **58**, 1801–1814, doi:10.1175/1520-0469(2001)058<1801:MAVCOA>2.0.CO;2.

——, and ——, 2001b: Effects of convective heating on movement and vertical coupling of tropical cyclones: A numerical study. *J. Atmos. Sci.*, **58**, 3639–3649, doi:10.1175/1520-0469(2001)058<3639:EOCHOM>2.0.CO;2.

Yeh, T.-C., and R. L. Elsberry, 1993a: Interaction of typhoons with the Taiwan topography. Part I: Upstream track deflection. *Mon. Wea. Rev.*, **121**, 3193–3212, doi:10.1175/1520-0493(1993)121<3193:IOTWTT>2.0.CO;2.

——, and ——, 1993b: Interaction of typhoons with the Taiwan topography. Part II: Continuous and discontinuous tracks across the island. *Mon. Wea. Rev.*, **121**, 3213–3233, doi:10.1175/1520-0493(1993)121<3213:IOTWTT>2.0.CO;2.

Zehnder, J. A., 1993: The influence of large-scale topography on barotropic vortex motion. *J. Atmos. Sci.*, **50**, 2519–2532, doi:10.1175/1520-0469(1993)050<2519:TIOLST>2.0.CO;2.

——, and M. J. Reeder, 1997: A numerical study of barotropic vortex motion near a large-scale mountain range with application to the motion of tropical cyclones approaching the Sierra Madre. *Meteor. Atmos. Phys.*, **64**, 1–19, doi:10.1007/BF01044127.